

See discussions, stats, and author profiles for this publication at:
<https://www.researchgate.net/publication/273061353>

Coupling of South and East Asian Monsoon Precipitation in July–August

ARTICLE *in* JOURNAL OF CLIMATE · JUNE 2015

Impact Factor: 4.44 · DOI: 10.1175/JCLI-D-14-00393.1

READS

50

3 AUTHORS, INCLUDING:



Jesse Alexander Day

University of California, Berkeley

3 PUBLICATIONS 14 CITATIONS

SEE PROFILE

Coupling of South and East Asian Monsoon Precipitation in July–August*

JESSE A. DAY AND INEZ FUNG

Department of Earth and Planetary Science, University of California, Berkeley, Berkeley, California

CAMILLE RISI

Laboratoire de Météorologie Dynamique, CNRS, Paris, France

(Manuscript received 19 May 2014, in final form 12 February 2015)

ABSTRACT


The concept of the “Asian monsoon” masks the existence of two separate summer rainfall régimes: convective storms over India, Bangladesh, and Nepal (the South Asian monsoon) and frontal rainfall over China, Japan, and the Korean Peninsula (the East Asian monsoon). In addition, the Himalayas and other orography, including the Arakan Mountains, Ghats, and Yunnan Plateau, create smaller precipitation domains with abrupt boundaries. A mode of continental precipitation variability is identified that spans both South and East Asia during July and August. Point-to-point correlations and EOF analysis with Asian Precipitation–Highly-Resolved Observational Data Integration Toward Evaluation of the Water Resources (APHRODITE), a 57-yr rain gauge record, show that a dipole between the Himalayan foothills (+) and the “monsoon zone” (central India, –) dominates July–August interannual variability in South Asia, and is also associated in East Asia with a tripole between the Yangtze corridor (+) and northern and southern China (–). July–August storm tracks, as shown by lag–lead correlation of rainfall, remain mostly constant between years and do not explain this mode. Instead, it is proposed that interannual change in the strength of moisture transport from the Bay of Bengal to the Yangtze corridor across the northern Yunnan Plateau induces widespread precipitation anomalies. Abundant moisture transport along this route requires both cyclonic monsoon circulation over India and a sufficiently warm Bay of Bengal, which coincide only in July and August. Preliminary results from the LMDZ version 5 (LMDZ5) model, run with a zoomed grid over Asia and circulation nudged toward the ECMWF reanalysis, support this hypothesis. Improved understanding of this coupling may help to project twenty-first-century precipitation changes in East and South Asia, home to over three billion people.

1. Introduction

The word monsoon, once used to denote the winds over the Arabian Sea that reverse seasonally, has migrated in meaning over the centuries to refer to the

accompanying period of high rainfall. From June to September, heavy rains over the Indian Subcontinent sustain agriculture ([Gadgil and Gadgil 2006](#)) and bring devastating floods. In turn, peak rainfall intervals in other regions are also referred to as monsoons, most occurring during the summer months of peak insolation (the East Asian, African, North American, and Australian monsoons) but not all (the East Asian winter monsoon). The South and East Asian monsoons are often referred to jointly as the Asian summer monsoon, even though they differ in month of onset and decay, precipitation amount, diurnal cycle of rainfall, and fraction of local yearly rainfall supplied ([Zhou et al. 2008](#); [Molnar et al. 2010](#); [Biasutti et al. 2012](#)).

The core months of the South Asian monsoon (July and August) together deliver over 50% of yearly precipitation to most of India and Nepal, and upward of

 Denotes Open Access content.

* Supplemental information related to this paper is available at the Journals Online website: <http://dx.doi.org/10.1175/JCLI-D-14-00393.s1>.

Corresponding author address: Jesse Day, Department of Earth and Planetary Science, College of Letters and Science, University of California, Berkeley, 307 McCone Hall, Berkeley, CA 94720.
E-mail: jessed@berkeley.edu

DOI: 10.1175/JCLI-D-14-00393.1

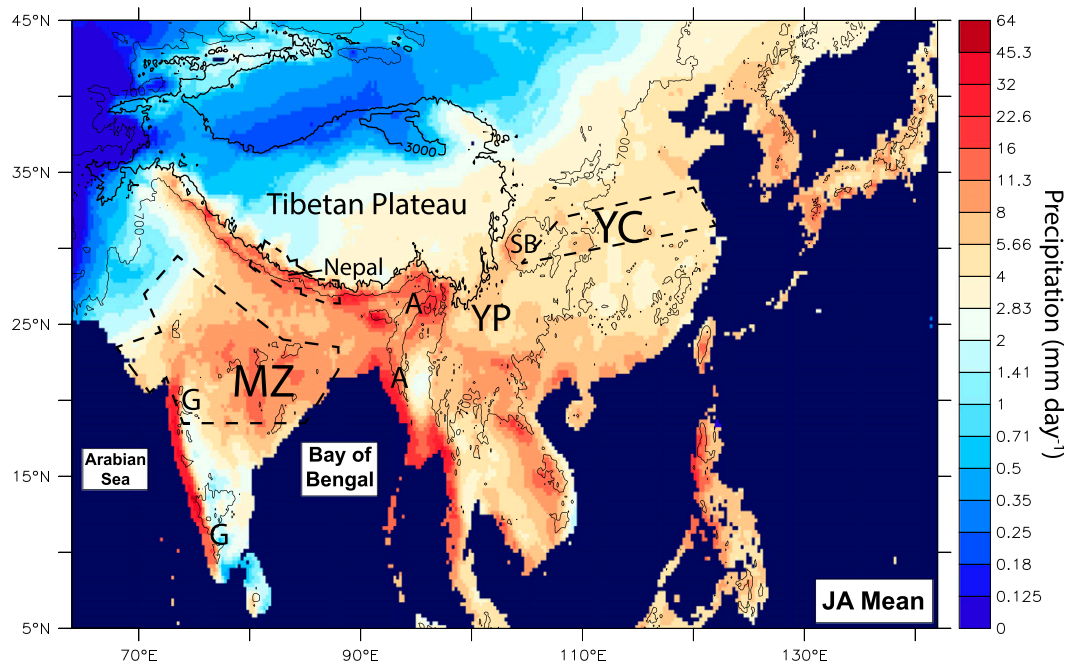


FIG. 1. July–August mean precipitation from APHRODITE (mm day^{-1} ; 1951–2007) plotted with a logarithm base 2 color scale. Topography contours of 700- and 3000-m elevation are superimposed (thin and thick contours, respectively). No data are available over water (deep blue shading) since APHRODITE is a composite of station data. Important regions are abbreviated as MZ (monsoon zone) and YC (Yangtze corridor). Key topographic features are labeled as follows: A for Arakan Mountains, G for Ghats, YP for Yunnan Plateau, and SB for Sichuan basin.

20 mm day^{-1} of rainfall to coastal Bangladesh, according to Asian Precipitation–Highly-Resolved Observational Data Integration toward Evaluation of the Water Resources (APHRODITE) rain gauge data (described below). In summer, episodes of convective storms last for several weeks at a time, regulated by a strong diurnal cycle (Romatschke and Houze 2011), and are interspersed by rainfall hiatuses of several days known as monsoon breaks (Krishnan et al. 2000). A core swath of central India including the states of Madhya Pradesh, Chhattisgarh, and Odisha, previously named the “monsoon zone” by Gadgil (2003), receives about 10 mm day^{-1} of rainfall averaged over summer (shown in Fig. 1). Daily totals reach as much as 50 mm day^{-1} in Meghalaya north of Bangladesh. The season of intense rainfall starts abruptly, first over southern India in May, next over the monsoon zone in June, and then over northern India in July, and ends over most of India by September. Traditionally, these characteristics are attributed to strong contrast between the low thermal capacity of land and high thermal capacity of the surrounding ocean, a theory dating back to the original study of the monsoon by Halley (1686). However, it has long been known that surface temperature over India maximizes in May–June, well ahead of peak rainfall (Gadgil 2003). Twentieth- and twenty-first-century researchers have invoked an alternative thermal argument, which

emphasizes the intense summer heating of the high Tibetan Plateau as the primary driver of the continental-scale Asian monsoon (Yeh et al. 1959; Li and Yanai 1996; Wu et al. 2007). However, Rajagopalan and Molnar (2013) found that heating of the Tibetan Plateau (measured by near-surface moist static energy) is correlated with Indian rainfall before and after the monsoon (20 May–15 June and 1 September–15 October, respectively), but uncorrelated during its peak (15 June–31 August).

In recent years, a new body of work has strengthened our understanding of the fluid dynamics of the South Asian monsoon. The delay between peak solar forcing and rainfall response and the sudden onset of heavy rainfall have been ascribed to nonlinearity in Hadley cell transitions and reproduced in idealized models (Plumb and Hou 1992; Schneider and Bordoni 2008; Bordoni and Schneider 2008). Furthermore, according to the framework of subcloud moist static energy and convective quasi-equilibrium (Emanuel 1995; Privé and Plumb 2007a,b), the strong Indian monsoon exists primarily because the Himalayas shield India from cold inland air (Boos and Kuang 2010). The debate over the relative importance of Tibetan Plateau heating and topographic blocking continues in the literature (Wu et al. 2012; Boos and Kuang 2013; Qiu 2013).

The East Asian summer monsoon manifests unique characteristics compared to its South Asian counterpart

and other tropical monsoons. From early June to mid-July, a persistent but migrating zonal front over China, Japan, and the Korean Peninsula delivers about 30 mm day^{-1} of rain along its axis. This period of peak frontal activity is known in China as mei-yu season, in Japan as baiu season, and over the Korean Peninsula as changma season. The preferred position of the mei-yu front shifts northward during this season, with apparent jumps between preferred latitudes (Ding and Chan 2005). The current debate on the dynamics of mei-yu season rainfall centers around the relative importance of downstream advection of Tibetan Plateau heating (Sampe and Xie 2010) versus meridional energy convergence induced by topographic forcing of stationary eddies (Molnar et al. 2010; Chen and Bordoni 2014b). The mei-yu season generally supplies a lower percentage of yearly rainfall to East Asia compared with the South Asian monsoon: cumulative May–July rainfall constitutes under 50% of yearly rainfall in southern China, and at most 70% in the northeast (from APHRODITE). The yearly rainfall climatology of China also includes the East Asian “winter monsoon” (Jhun and Lee 2004), spring persistent rains (Tian and Yasunari 1998) and post-mei-yu rainfall [cf. “midsummer” in Kosaka et al. (2011)]. Finally, many authors have reported a “south flood–north drought” trend in the East Asian summer monsoon since the late 1970s (Gong and Ho 2002; Ding et al. 2008), attributed either to anthropogenic influence or natural variability (Song et al. 2014; Lei et al. 2014).

In summary, the South and East Asian monsoons share a name, but they are dissimilar in phenomenology and dynamics. Summer daily rainfall rates in India are about twice those of East Asia (10 mm day^{-1} over the monsoon zone and Himalayan foothills versus 5 mm day^{-1} over central China; Fig. 1). In the climatological mean, mei-yu rainfall in central China peaks around 15–25 June. Rainfall rates over India increase sharply around this time, but the climax of the South Asian monsoon occurs only a month later during the period 15 July–5 August. Summer storms over the Bay of Bengal show a weak midday peak, and storm occurrence along the Himalayan foothills peaks at night when upslope winds reverse (Romatschke and Houze 2011), whereas station data from China show a complex diurnal cycle of precipitation that varies regionally (Zhou et al. 2008). The physics of the South Asian monsoon have more in common with other summer circulations such as the African, North American, or Australian monsoons than with the East Asian monsoon (Rodwell and Hoskins 2001). The most pertinent shared characteristic of the Asian monsoon may instead be sociological: the reliance of the region’s dense population on heavily stressed freshwater resources that may be vulnerable to twenty-first-century

climate change (Gleeson et al. 2012; Jiménez Cisneros et al. 2014).

The South and East Asian monsoons, aside from their large-scale differences, each contain many precipitation subdomains. Precipitation has a correlation length scale of about 300 km (Dai et al. 1997), shorter than that of temperature (about 1000 km) and eddies (about 700 km) (Hansen and Lebedeff 1987; Barnes and Hartmann 2012). In the South Asian monsoon region, orography can induce transitions across short distances, as seen previously in Xie et al. (2006) and Biasutti et al. (2012) and in our Fig. 1. The Himalayas, less than 100-km wide and above 5-km high, function as a barrier that separates heavy precipitation at the Himalayan foothills ($\sim 30 \text{ mm day}^{-1}$) from the arid Tibetan Plateau ($< 3 \text{ mm day}^{-1}$). Lower ranges such as the Arakan Mountains on the western border of Myanmar¹ ($\sim 2000 \text{ m}$ of altitude) and the Ghats ($\sim 700 \text{ m}$) anchor coastal bands of abundant rainfall ($> 25 \text{ mm day}^{-1}$) on their windward western slope through a combination of forced ascent and diabatic feedback Xie et al. (2006), and also induce aridity ($2\text{--}5 \text{ mm day}^{-1}$) on their leeward eastern flank.

We focus throughout this work on the impact on rainfall of another region of high topography, the Yunnan Plateau, a north–south spur of the southeastern Tibetan Plateau that descends from over 3 km of altitude in northern Myanmar and southern China to below 1 km farther south. The Yunnan Plateau anchors rainfall rates of $20\text{--}30 \text{ mm day}^{-1}$ to its west, but only about 6 mm day^{-1} on its summit (see Fig. 1). Thus, the Yunnan Plateau functions as a barrier on the climatological distribution of summer rainfall, similar to other regional orography. However, in our subsequent results, we find that deviations from mean rainfall (i.e., monthly rainfall anomalies) demonstrate a spatial signature that crosses the Yunnan Plateau in July and August. Not only are northeastern India and the Sichuan basin on either side of the Yunnan Plateau linked, but points across the entire Asian monsoon domain show robust correlation of rainfall anomalies in these months, even when separated by thousands of kilometers. The goal of the rest of this work is to investigate the coupled interannual variability of the South and East Asian monsoons, and the dynamic role of intervening high topography in this linkage.

In section 2, we introduce APHRODITE, a 57-yr historical precipitation record used in our analysis.

¹The crescent-shaped mountains on Myanmar’s western flank include the Patkai Hills to the north, the Chin Hills in their center, and the Arakan Mountains to the south. In the interest of brevity, we hereafter use the term Arakan Mountains to refer to the entire band of high topography (marked by an A in Fig. 1).

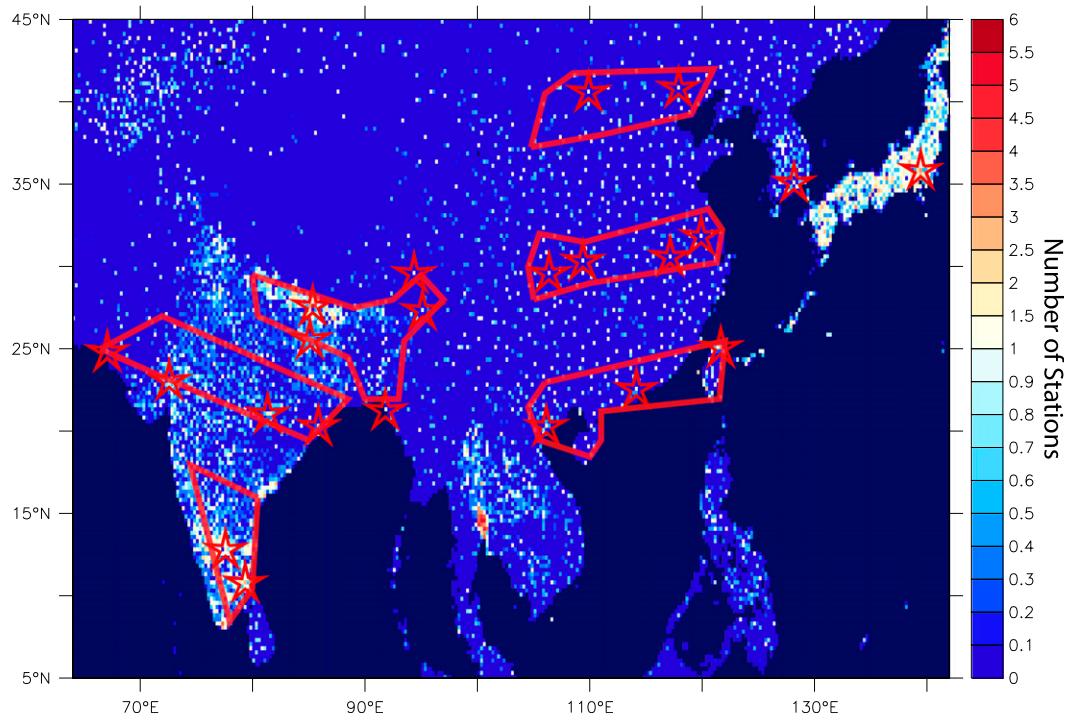


FIG. 2. Mean station coverage (STN) in APHRODITE (1951–2007), with the 22 reference points (stars) and six regions (Himalayan foothills, monsoon zone, southern India, southern China, Yangtze corridor, and northern China) used to calculate correlations and agreement maps.

Section 3 shows the results of point-to-point correlations and uses an agreement map methodology to display their associated spatial pattern. In section 4, we use empirical orthogonal function (EOF) analysis over different regions and months to further study the interannual variability of Asian precipitation. Section 5 proposes several local rainfall indices that replicate the large-scale signal. Section 6 investigates storm tracks in the Asian monsoon. Section 7 proposes a mechanism that can explain our findings. In section 8, we provide a first test of our hypothesis using results from the LMDZ model. Section 9 offers some concluding remarks.

2. APHRODITE

a. A rain gauge dataset for Asia

In this study, we use a compilation of rain gauge data from weather stations, APHRODITE (Yatagai et al. 2012). The APHRO_MA_V1101 product includes 57 years (1951–2007) of daily precipitation (PRECIP product in units of mm day^{-1}) and station coverage (RSTN product) on either a $0.25^\circ \times 0.25^\circ$ grid (roughly 25-km spacing) or $0.5^\circ \times 0.5^\circ$ grid (~ 50 -km spacing) within 15°S – 55°N , 60° – 150°E . Subsequent analysis uses the $0.25^\circ \times 0.25^\circ$ product unless otherwise indicated. Rainfall values are only available over land. Original

station data are provided by national meteorological services, and do not always include all extant stations. Erroneous values are excised via a series of quality control algorithms. The data are then transferred to a fine $0.05^\circ \times 0.05^\circ$ grid (roughly 5-km spacing) via topography-dependent spline interpolation, and finally upscaled to the $0.25^\circ \times 0.25^\circ$ and $0.5^\circ \times 0.5^\circ$ gridded products available to users. A complete description of the assimilation procedure is available in Yatagai et al. (2012). RSTN is expressed as the percentage of $0.05^\circ \times 0.05^\circ$ subcells that contain a station within each $0.25^\circ \times 0.25^\circ$ cell (cells usually contain either 0 or 1 station, such that RSTN mostly equals 0% or 4%). We re-express RSTN as a number of stations STN using the definition $\text{STN} = \text{RSTN}/4$ (shown in Fig. 2).

APHRODITE roughly agrees with existing precipitation datasets, such as the $1^\circ \times 1^\circ$ dataset of Rajeevan et al. (2006), but features improved station coverage and accuracy in regions with sharp topography gradients, in particular around the Himalayan foothills and the Ghats (Yatagai et al. 2012). Analysis of station data is challenging because the distribution of stations is spatially uneven and changes with time. There may also be inherent flaws in measurement as a result of potential equipment bias and discrepancies in collection intervals between countries. However, alternative precipitation

datasets suffer from weaknesses of their own. Reanalysis products such as NCEP–DOE fail to reproduce the intensity and spatial pattern of observed precipitation during monsoon season (Peña-Arancibia et al. 2013). ERA-40 and the newer ERA-Interim product reproduce the seasonal cycle of rainfall distribution on the Tibetan Plateau, but struggle with the magnitude of rainfall relative to rain gauge and hydrological observations (Tong et al. 2014). Satellite precipitation products overestimate low precipitation rates and underestimate heavy precipitation, and also perform poorly in arid regions (Gao and Liu 2013). TRMM satellite data struggle with quantification of intense precipitation over land (Iguchi et al. 2009). The TRMM 3B42v6 product was found to perform well over low terrain in China but worse over high terrain (Zhao and Yatagai 2014). Mergers of rain gauge, satellite, and reanalysis data exist (Peña-Arancibia et al. 2013; Shen et al. 2014), but for simplicity our analysis relies only on APHRODITE data.

b. Normalized monthly precipitation anomalies

The daily PRECIP time series $d(x, y, \text{day}, \text{year})$ at each terrestrial point (360×280 points per day for 20819 days) are converted into monthly precipitation rates $P(x, y, \text{month}, \text{year})$ in order to attenuate high-frequency variability. Choices of 15-, 10- (decad), and 5-day (pentad) bins were also tested, with similar results. To compare points with different means and standard deviations of rainfall, we find the precipitation anomaly in each month relative to monthly mean, defined as P' , and also the normalized anomaly P'' , obtained by dividing P' by the 57-yr standard deviation σ_{mth} of precipitation in that month (mth). Therefore P'' is in units of standard deviation. The means and standard deviations used to calculate P' and P'' are different at each point (x, y) . Equivalently in equation form we define the following variables, where σ denotes standard deviation:

$$\begin{aligned} d(x, y, \text{day}, \text{year}) \\ = 57\text{-yr daily time series at point } (x, y), \end{aligned}$$

$$\begin{aligned} P(x, y, \text{month}, \text{year}) \\ = d(x, y, \text{day}, \text{year}), \text{ converted to monthly mean rate,} \end{aligned}$$

$$\overline{P}_{\text{mth}}(x, y) = \overline{P(x, y, \text{mth}, \text{year})}^{57\text{yr}} \quad \text{for } \text{mth} = 1, \dots, 12,$$

$$\sigma_{\text{mth}}(x, y) = \sigma[P(x, y, \text{mth}, \text{year})] \quad \text{for } \text{mth} = 1, \dots, 12,$$

$$P'(x, y, \text{mth}, \text{year}) = P(x, y, \text{mth}, \text{year}) - \overline{P}_{\text{mth}}(x, y), \quad \text{and}$$

$$P''(x, y, \text{mth}, \text{year}) = \frac{P'(x, y, \text{mth}, \text{year})}{\sigma_{\text{mth}}(x, y)}.$$

In all subsequent analysis, the normalized anomaly from each month is treated as a separate time point. For instance, when we discuss a July–August (JA) anomaly time series over all 57 years, we refer to a time series with 114 points: 57 July and 57 August points. Similarly, a May–October (MJJASO) time series from 1951 to 2007 has $57 \times 6 = 342$ independent time points. The autocorrelation of normalized rainfall anomalies between successive months is low, which supports the claim that each month in a normalized rainfall anomaly time series represents an independent observation.

c. Reference points and regions

In section 3, we focus on the P'' monthly normalized rainfall anomaly time series at 22 reference points with good station coverage over the 57-yr time period (Table 1). The nearest urban agglomeration to each point is listed for illustration. The results from section 3 are robust to the replacement of chosen points with other nearby points. We also designate six reference regions, three each over South and East Asia (Fig. 2). In South Asia, the three regions are the Himalayan foothills and Bangladesh, the monsoon zone, as defined in the introduction, and southern India east of the Ghats. The three regions in East Asia are southern China (which also includes Taiwan and northern Vietnam), the “Yangtze corridor” stretching from Sichuan to Shanghai, and northern China along the Yellow River.

The P'' time series are calculated for each of the 22 points and six regions. All 22 reference points belong to one of the six regions, except for a point each in South Korea (Jinju) and Japan (Tokyo). Both of these points are well correlated with the Yangtze corridor in summer (Figs. 3 and 4), but the correlation of the rest of Japan and South Korea with the Yangtze corridor is weak. Precipitation anomalies within each region are highly correlated. Regional time series are defined as $P''_{\text{region}} = \overline{P''(x, y)}^{x, y}$, the mean standardized anomaly over the region, and are used to confirm that our results are not sensitive to the exact choice of reference points. We could also first construct a regional time series $P_{\text{region}} = \overline{P(x, y)}^{x, y}$ and calculate the corresponding mean and standard deviation, but such a procedure emphasizes points with high variance. In practice, the two methods produce highly similar time series except for the Himalayan foothills and Bangladesh time series, which includes very rainy points near Meghalaya.

TABLE 1. The 22 reference points used in the point-to-point comparisons and agreement map.

| Region | No. | Nearest city | Lon | Lat | JA precip (mm day ⁻¹) | Std dev | STN |
|---|-----|------------------------|---------|--------|--------------------------------------|---------|------|
| Himalayan foothills and Bangladesh | 1 | Chittagong | 91.9°E | 22.4°N | 16.55 | 6.58 | 0.88 |
| | 2 | Kathmandu | 85.4°E | 27.6°N | 12.34 | 3.33 | 5.09 |
| | 3 | Patna | 85.1°E | 25.6°N | 7.78 | 2.92 | 2.42 |
| | 4 | Eastern Assam | 95.1°E | 27.4°N | 12.62 | 3.27 | 1.04 |
| | 5 | Nyingchi | 94.4°E | 29.6°N | 3.71 | 1.47 | 1.28 |
| Monsoon zone | 6 | Bhubaneswar | 85.9°E | 20.4°N | 10.06 | 3.04 | 1.98 |
| | 7 | Durg | 81.4°E | 21.1°N | 9.26 | 2.98 | 1.83 |
| | 8 | Ahmedabad | 72.6°E | 23.1°N | 7.11 | 3.85 | 1.74 |
| | 9 | Karachi | 67.1°E | 24.9°N | 1.68 | 2.01 | 0.86 |
| Southern India | 10 | Bangalore | 77.6°E | 12.9°N | 3.04 | 1.78 | 1.89 |
| | 11 | Kumbakonam | 79.4°E | 10.9°N | 2.29 | 1.62 | 2.94 |
| Southern China | 12 | Nam Dinh | 106.1°E | 20.4°N | 7.64 | 3.80 | 1.56 |
| | 13 | Shenzhen | 114.1°E | 22.6°N | 9.78 | 4.41 | 1.01 |
| | 14 | Taipei | 121.6°E | 25.1°N | 6.59 | 4.62 | 3.36 |
| Yangtze corridor, Korean Peninsula, and Japan | 15 | Chongqing | 106.4°E | 29.6°N | 4.41 | 2.15 | 1.49 |
| | 16 | Enshi | 109.4°E | 30.4°N | 5.80 | 3.09 | 1.32 |
| | 17 | Anqing | 117.1°E | 30.6°N | 4.58 | 3.03 | 1.42 |
| | 18 | Changzhou | 119.9°E | 31.9°N | 4.39 | 2.37 | 1.14 |
| | 19 | Jinju (South Korea) | 128.1°E | 35.1°N | 7.66 | 4.10 | 1.67 |
| | 20 | Tokyo | 139.4°E | 35.9°N | 5.35 | 2.86 | 3.33 |
| Northern China | 21 | Baotou | 109.9°E | 40.6°N | 2.47 | 1.26 | 1.08 |
| | 22 | Chengde | 117.9°E | 40.9°N | 4.50 | 1.99 | 1.98 |

The density of observations in APHRODITE varies widely (Fig. 2). Japan features a nationwide dense station network, whereas almost no data are available from the western Tibetan Plateau. Several of our reference points (Nyingchi on the eastern Tibetan Plateau and Karachi at the edge of the Thar Desert) contain the only station within a 100-km radius and should be interpreted with caution. Station density also changes with time. The number of available stations in India drops abruptly from over 3000 during 1951–70 to <1000 in 1971 and thereafter. In China, the number of stations remains roughly constant in time (~700 stations). To limit the impact of station heterogeneity in space and time, we select reference points with good data and adjust the methodology of our EOF analysis to account for station coverage.

3. Spatial coherence of precipitation anomalies

a. Point-to-point correlations

1) FORMULA

Between two monthly precipitation time series P_1 and P_2 , we define the Pearson product–moment correlation coefficient, also referred to as the correlation coefficient r , which also equals the mean product of monthly normalized anomaly time series P'_1 and P'_2 :

$$r(P_1, P_2) = \frac{\sum[(P_1 - \overline{P_1})(P_2 - \overline{P_2})]}{n\sigma(P_1)\sigma(P_2)} = \frac{\overline{(P_1 - \overline{P_1})(P_2 - \overline{P_2})}}{\sigma(P_1)\sigma(P_2)} = \overline{P'_1 P'_2}.$$

This formula assumes that monthly rainfall anomalies follow a normal distribution, whereas daily and monthly rainfall rates are more accurately described by a gamma distribution, both in Asia and elsewhere (Mooley 1973; Aksoy 2000; Husak et al. 2007). Monthly anomalies at the 22 reference points approach a normal distribution except at Karachi, where the standard deviation exceeds the mean (Table 1). This results from occasional monthly surges of up to 8 mm day⁻¹ superimposed on a hyperarid (1 mm day⁻¹) background. We persist in using the standard formula for r anyway in the interest of simplicity.

2) RESULTS

We focus on summer rainfall, and in particular July–August when the South Asian monsoon peaks. In Fig. 3, we show the 57-yr intercorrelation of monthly rainfall anomalies P'' for each of our 22 reference points in July–August (114 time points; bottom left), and also for summer half-year months (MJJASO, 342 time points; top right). Correlations significant at a 95% (99%) confidence levels are marked with single (double) cross hatching, estimated using Student's t test with degrees of

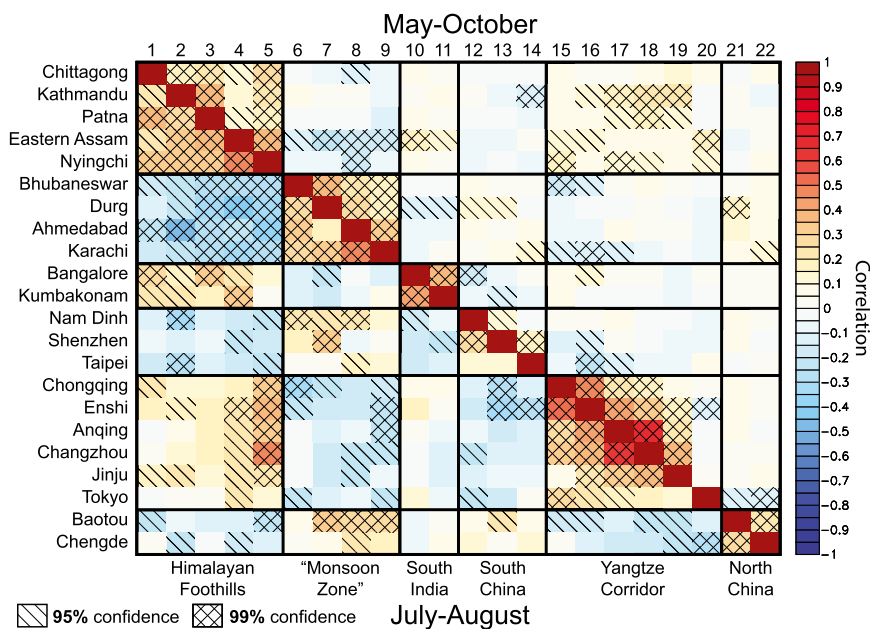


FIG. 3. Correlation coefficient r of normalized monthly precipitation anomaly time series P'' between each of the 22 reference points for the years 1951–2007. Each monthly anomaly is treated as an independent time point: (bottom left) July–August (114 time points) and (top right) May–October (342 time points). Confidence levels above 95% and 99% are indicated by single and double cross hatching, respectively. Given degrees of freedom n , the threshold for significance is listed: July–August ($n = 112$) 95% (99%), $|r| > 0.184$ (0.240) and May–October ($n = 340$) 95% (99%), $|r| > 0.106$ (0.139). Shared autocorrelation between monthly rainfall anomaly time series is small and does not affect the number of effective degrees of freedom. Region-to-region correlations reproduce point-to-point results closely (not shown).

freedom $n = 112$ for July–August and $n = 340$ for summer half-year months. The number of effective degrees of freedom n in cross correlation is reduced if both time series share nonzero autocorrelation at a particular time lag (Livezey and Chen 1983), which can raise the threshold for statistical significance. However, the shared autocorrelation of both JA and MJJASO rainfall time series is found to be very low.

Intraregional correlations are generally strong for both July–August and for summer half-year months. In July–August, statistically significant correlations are also found between points in different regions, even though the amplitude and seasonality of summer rainfall vary greatly between sites, as noted by Wang and LinHo (2002). For instance, July–August mean rainfall varies by an order of magnitude between Chittagong ($16.55 \text{ mm day}^{-1}$) and Karachi (1.68 mm day^{-1}). Mean rainfall peaks in June in southern China, July–August in northern India, and fall in southern India. Nevertheless, July–August precipitation anomalies are coherent over more than 5000 km, from Tokyo and Karachi ($r = -0.23$, significant at a 95% level) to pairs of points in between, whereas significant correlations during summer half-year months (May–October) are mostly limited to pairs of points within the same region.

To verify the robustness of these findings, we reproduced Fig. 3 using different combinations of summer months, including June–September (JJAS). The choice of July–August was found to maximize interregional correlation strength. Correlations were also calculated between regional time series (not shown). Their magnitude mostly exceeds the 99% confidence level, with sign of correlation matching the overall pattern observed in Fig. 3. The preceding analysis implicitly assumes that the spatial correlation fields associated with a positive and negative rainfall anomaly are mirror images of one another. This is not guaranteed to be true. For instance, the spatial patterns of El Niño and La Niña teleconnections are not exact inverses (Hoerling et al. 1997). To test for this possibility, we compiled two composites of years: a “wet composite” only including the five most positive July–August anomaly years at Kathmandu and a “dry composite” with the five most negative years. We again reproduced Fig. 3 with each composite, and obtained similar results for both composites (not shown).

The strongest July–August interregional correlation is a dipole between points in the Himalayan foothills (hereinafter defined as +) and the monsoon zone (defined as -) ($r = -0.59$ using regional time series). This

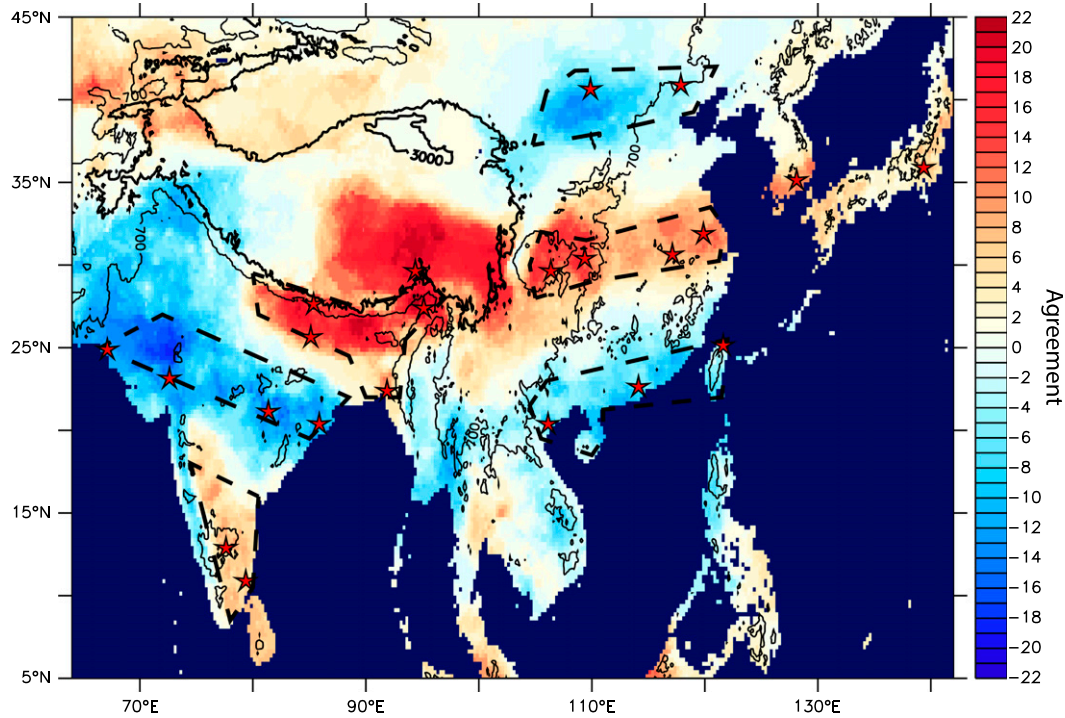


FIG. 4. Agreement map $A(x, y)$ of July–August rainfall anomalies predicted by all 22 reference points, calculated using method described in section 3b, with 3000- and 700-m topography isolines superimposed (thick and thin lines, respectively) and reference points marked with red stars.

dipole structure over South Asia recurs throughout this study. Southern India also simultaneously tends to experience positive anomalies ($r = 0.52$ with the Himalayan foothills and -0.20 with the monsoon zone). This spatial pattern has been known to the Indian Meteorological Department since the 1960s (Krishnamurthy and Shukla 2000). In East Asia, a tripole pattern emerges with precipitation increases over the Yangtze corridor, Korean Peninsula, and Japan and corresponding decreases over southern China, Taiwan, and northern Vietnam, as well as a smaller decrease in northern China (from north to south: $-$, $+$, $-$). This pattern is also found in previous studies (Ding et al. 2008) and should not be conflated with the variability of the mei-yu front, since the mei-yu season ends sometime in mid-July (Wang and LinHo 2002). The relatively low correlation of reference points in northern China with other regions may reflect chaotic forcing from the westerlies in that region (Kosaka et al. 2012). Finally, Fig. 3 reveals that many points in South Asia are significantly correlated to points in East Asia during July–August. In particular, anomalies over the Himalayan foothills correspond to anomalies over the Yangtze corridor ($r = 0.35$ using regional time series). Previous authors have investigated potential connections between the South and East Asian summer monsoons (Lau et al. 2000; Liu and Ding 2008).

Krishnan and Sugi (2001) found a correlation exceeding a 95% significance level between June–July integrated rainfall over the monsoon zone and baiu intensity (the mei-yu front over Japan). A similar result is visible in Fig. 3. The link between the two regions is investigated in following sections.

b. Agreement map

According to Fig. 3, July–August interannual precipitation anomalies are correlated across large distances. To elucidate their spatial structure, we employ an agreement map methodology that compares the pattern of anomalies predicted by each of our 22 reference points. The agreement $A(x, y)$ is defined via the following formulas:

$$R_i(x, y) = r[P_i, P(x, y)],$$

$$S_i(x, y) = R_i(x, y) \operatorname{sgn}[r(P_i, P_{\text{Nepal}})],$$

$$Q_i(x, y) = \begin{cases} \operatorname{sgn}[S_i(x, y)], & \text{if } |S_i(x, y)| > 0.2 \\ 0, & \text{if } |S_i(x, y)| < 0.2 \end{cases}, \quad \text{and}$$

$$A(x, y) = \sum_i Q_i(x, y).$$

For each reference point i with local time series P_i , we find the correlation of P_i with $P(x, y)$ for all x and y during

July–August, defined as $R_i(x, y)$ (360×280 points for 114 months). To compare two different $R_i(x, y)$ maps, they must be defined with the same sign convention. We choose Kathmandu (27.6°N , 85.4°E , reference point 2) as our frame of reference because of its strong correlations with other reference points and high station coverage. If reference point i is negatively correlated with Kathmandu $r(P_i, P_{\text{Nepal}}) < 0$, we flip the sign of R_i . The R_i values with adjusted sign are defined as $S_i(x, y)$ and can now be directly compared. The choice of other reasonable reference frames leads to similar results. We then isolate regions of robust correlation in each S_i with a magnitude threshold. We define $Q_i(x, y)$ as the sign of $S_i(x, y)$ (+1 or -1) if the magnitude of S_i at that point exceeds 0.2, and 0 otherwise. The choice of 0.2 as threshold (roughly a 97% confidence level using degrees of freedom $n = 112$) is arbitrary, and changing the threshold does not alter the overall pattern seen in Fig. 4. Finally, the agreement $A(x, y)$ is obtained by summing all Q_i . A high magnitude of A at a point (x, y) indicates that a strong anomaly is predicted at (x, y) given the prior observation of an anomaly at each reference point.

Figure 4 shows a July–August agreement map using all 57 years. We also tested agreement maps using the composites of wet and dry years defined in section 3a, and find that results are not substantially altered in either case except for increased noise due to smaller sample size (not shown). A weak branch of positive anomaly extends northward from the Bay of Bengal, on the western flank of the Arakan Mountains. When this branch reaches the Himalayas, it strengthens and bifurcates into northwestward and northeastward trajectories. The northwestward branch runs along the Himalayan foothills to Nepal without encroaching onto the Tibetan Plateau. The northeastward branch follows a channel between the Himalayas to the north and the Arakan Mountains to the southeast, fills the northeastern notch of the Himalayan foothills, and spills onto the southeastern Tibetan Plateau. This branch also crosses the northern Yunnan Plateau into Sichuan and the Yangtze corridor of central China, and stretches weakly across South Korea and Japan. The tilt of this band resembles that of the mei-yu front, even though mei-yu season in central China ends during July.

In some places, sharp transitions between regions of positive and negative anomaly are collocated with orography, similar to the steep gradients in mean precipitation in Fig. 2. For instance, both the Arakan Mountains and Ghats divide regions of opposite sign on their western and eastern flanks (+ and $-$ for the former and $-$ and + for the latter, respectively). In contrast to these other topographic barriers, a continuous band of positive anomaly connects the southeastern

Tibetan Plateau (~ 4 km of altitude) and northern Yunnan Plateau (~ 3 km) with the low terrain of Bangladesh and the Himalayan foothills. It is also known from observation of $\delta^{18}\text{O}$ isotopes in rainfall that moisture in summer storms on the southern and southeastern Tibetan Plateau originates from the Bay of Bengal (Yao et al. 2009; Gao et al. 2011; Yang et al. 2012). Therefore, the Himalayas to the west of Nepal (80° – 86°E) function as an apparent barrier, but the eastern half of the Himalayas (east of 86°E) does not. The role of topography in blocking or allowing flow is not immediately explicable within existing monsoon theory. We propose a hypothesis explaining these features in section 7.

4. Empirical orthogonal function analysis

a. Technique

We seek to confirm the results of our point-to-point correlations and agreement map method using an alternative technique. EOF analysis is commonly used in climate studies to reveal leading modes of variability in a set of time series without the assumption of periodicity or preselected basis functions. This is achieved by finding the eigenmodes of the correlation or covariance matrix of all of the time series with one another (Lorenz 1956; Wilks 2006). Each eigenmode consists of a paired space and time component, hereafter referred to as spatial and temporal EOFs. These modes are ordered by the percentage of total variance that each explains, and typically a subset of several important modes is isolated. These are not guaranteed to have physical significance, but nonetheless can help to characterize a system. EOFs of precipitation have been calculated for India (Krishnamurthy and Shukla 2000) and China (Ding et al. 2008), but to our knowledge not for the entire Asian monsoon or with APHRODITE.

Normalized anomaly time series P'' (units of standard deviation) are used throughout our EOF analysis in order to weight anomalies at all points evenly. The interpolation algorithm used to compile APHRODITE provides daily data at every spatial point even if no stations are nearby. Without some adjustment for station coverage, the EOF technique can therefore generate spurious modes with high amplitude in areas with few true data, such as the western Tibetan Plateau and Taklamakan Desert. Therefore, we implement a method to include data only if a station is nearby, as indicated by the STN product. We define s as the fraction of days in each month where there is an operating station within 100 km of a point (x, y) . If $s < 0.5$, P'' at (x, y) is reported as missing for the month. Subsequently, if more than half of monthly values are missing over the 57 years, the point is omitted entirely from the calculation

of EOFs. This guarantees that all pairs of time series will overlap for at least one month according to the pigeonhole principle, permitting the calculation of their covariance. In practice, for Julys and Augusts from 1951 to 2007, 30.8% of time series overlap on all months, 90% of time series overlap on 75% of months, and 99.7% of time series overlap on at least 50% of months. Different proximity criteria for data inclusion were also tested, but the current 100-km criterion is sufficient to eliminate spurious modes. The resulting temporal EOFs do not include gaps because missing values are replaced with estimates that minimize expected error in a least squares sense, as described in the appendix of [Chelton and Davis \(1982\)](#).

In calculating EOFs, each monthly anomaly is treated as an independent time point, as described in [section 2](#) and consistent with the analysis in [section 3](#). EOFs are calculated for the months of June through September separately (57 time points), July–August (114 time points), each season [December–February (DJF), March–May (MAM), June–August (JJA), and September–November (SON); 171 time points] and for the summer and winter half-year months [MJJASO and November–April (NDJFMA) respectively; 342 time points]. In addition, July–August EOFs are found for the entire Asian monsoon region (“all Asia;” 5° – 45° N, 66° – 142° E) as well as India (10° – 30° N, 71° – 95° E) and China (20° – 40° N, 100° – 123° E) separately. The India and China subregions as defined each include parts of other countries (“India” includes Bangladesh, Nepal, Bhutan, western Myanmar, and southern Tibet, while “China” includes northern Vietnam and Laos), but are referred to by single country names for convenience. All-Asia EOFs are calculated at $0.5^{\circ} \times 0.5^{\circ}$ resolution and regional EOFs are calculated at $0.25^{\circ} \times 0.25^{\circ}$ resolution. Although APHRODITE also releases a $0.5^{\circ} \times 0.5^{\circ}$ product, the all-Asia EOFs are instead obtained by calculating s at $0.25^{\circ} \times 0.25^{\circ}$ resolution and then including one out of every two points in each direction. The calculation of EOFs at $0.5^{\circ} \times 0.5^{\circ}$ resolution produces very similar results to our procedure.

Preisendorfer’s “Rule N” ([Preisendorfer et al. 1981](#)) and the [North et al. \(1982\)](#) “rule of thumb” are used to assess statistical significance and independence of EOFs. The modes of rainfall variability described below are all statistically significant by Rule N. However, leading EOFs are generally not well separated, which indicates that their physical significance should be interpreted with caution. We also test the sensitivity of computed EOFs to varimax rotation ([Kaiser 1958](#)), which has been claimed to produce modes with greater physical significance ([Wilks 2006](#)).

b. Results

Leading modes of precipitation variability explain low percentages of variance relative to the leading modes of other atmospheric fields. For instance, the first EOF (EOF1) of global monthly rainfall, which is related to ENSO, explains only 6.3% of total variance ([Dai et al. 1997](#)). In South and East Asia, leading precipitation modes change greatly between seasons. During the winter half-year (NDJFMA), a north–south dipole with few local features dominates Asian precipitation variability (11.8% of variance explained; see Fig. S1a in the supplementary material). In fall (SON), the leading mode of all-Asia variability contrasts China with the Yunnan Plateau (8.6%; Fig. S1f). No statistically significant correlation is found between temporal EOF1s from different seasons, or between the summer and winter half-year EOF1 time series.

We begin by finding the leading all-Asia EOF of each month from June to September separately ([Fig. 5](#)). July EOF1 closely resembles August EOF1, with a slight meridional displacement visible over China (centered pattern correlation of $r = 0.7$), but [Fig. 5](#) shows that June and September EOF1s are both rather different. Furthermore, in July and August, EOF1 explains 10.4% and 12.9% of variance each, versus 9.9% and 8.7% in June and September respectively. June and September EOFs 2–4 are also distinct from July and August EOFs 2–4 (not shown). In summary, July and August show distinct behavior, which we further explore below through joint July–August EOFs ([Fig. 6](#)).

July–August all-Asia spatial EOF1 (9.4% of variance explained, [Fig. 6a](#)) closely resembles the agreement map in [Fig. 4](#). July–August spatial EOFs 2–4 ([Figs. 6b–d](#)) all also feature competition between the monsoon zone and the Himalayan foothills, and either a north–south tripole or dipole pattern in China. In particular, EOF3 resembles EOF1 in South Asia but with flipped sign in East Asia (spatial correlation in South Asia is 0.32 and in China is -0.31 ; obtained by centered pattern correlation). The tripole and dipole pattern over East Asia are similar to singular value decompositions (SVDs) 1 and 2 of East Asian summer rainfall in [Kosaka et al. \(2011\)](#). The first four all-Asia JA EOFs cumulatively account for 25.7% of total variance (9.4%, 6.8%, 5.2%, and 4.2% respectively).

The choice of a large region for EOF analysis may lead to mixing of independent modes ([Dai et al. 1997](#); [Wilks 2006](#)). Therefore, we repeat our EOF analysis of July–August rainfall for India and China separately ([Fig. 7](#)). India JA spatial EOF1 again displays a Himalayan foothills–monsoon zone dipole, and is almost identical to the South Asian portion of [Figs. 4](#) and [6a](#).

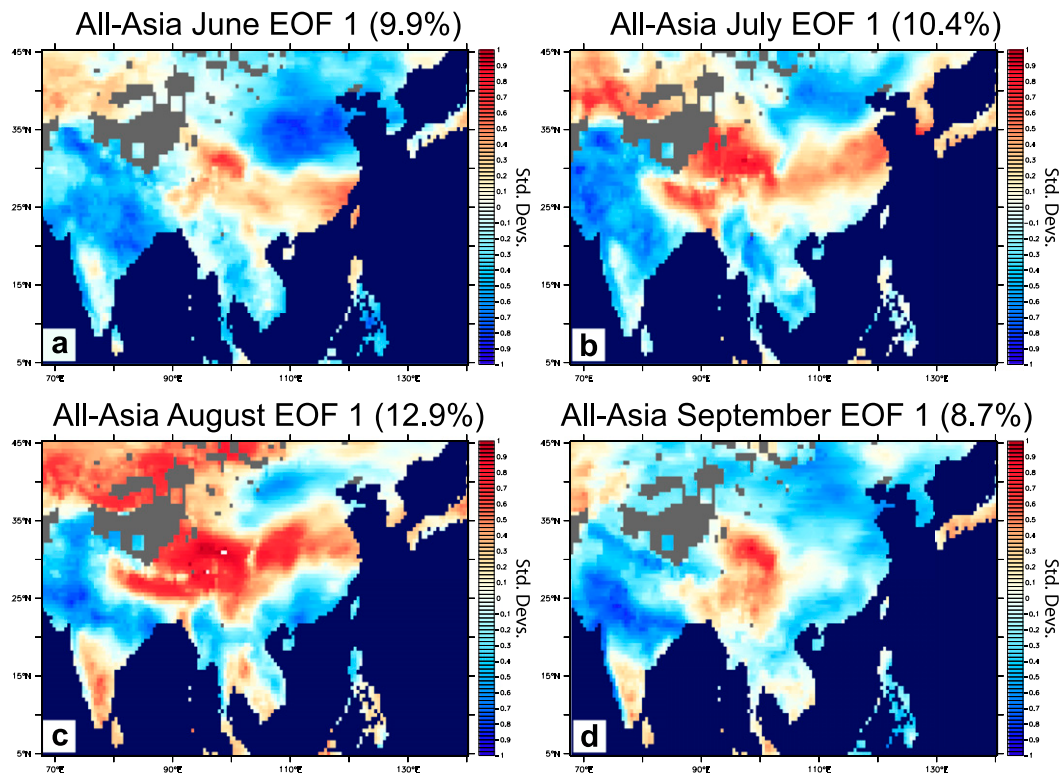


FIG. 5. EOF1 of normalized anomaly precipitation (std dev) computed separately for (a) June, (b) July, (c) August, and (d) September for the all-Asia region (5° – 45° N, 68° – 140° E) with $0.5^{\circ} \times 0.5^{\circ}$ resolution for 1951–2007. Percentage of variance explained by each EOF is listed in parentheses.

This mode dominates regional variability (22.5% of variance explained). Furthermore, spatial EOFs 2–5 also retain a similar dipole but shifted zonally or meridionally (not shown).

In China, three EOFs (hereafter referred to as C_1 , C_2 , and C_3) each explain over 10% of July–August variance, while no other mode surpasses 7%. Note that C_1 and C_2 both feature tilted zonal bands and meridional contrast (16.1% and 14.9% of variance explained), while C_3 contrasts low terrain in southern and eastern China with elevated regions inland (11.2%, not shown). Neither C_1 nor C_2 matches the China component of all-Asia JA spatial EOF1 or EOF2, hereafter referred to as AA_1 and AA_2 (in contrast to all-Asia EOFs 1 and 2, which refer to the spatial patterns over the full domain seen in Fig. 6). However, the application of a 45° rotation to the combination of C_1 and C_2 reproduces AA_1 and AA_2 very closely ($AA_1 = 0.59C_1 + 0.51C_2$, $AA_2 = -0.51C_1 + 0.55C_2$; coefficients obtained by correlation of temporal EOFs). This implies that both sets of EOFs (C_1/C_2 and AA_1/AA_2) describe the same variability.

Leading July–August all-Asia EOFs capture patterns of variability similar to those of regional EOFs, but also show an interregional coupling similar to Figs. 3 and 4.

Specifically, positive anomalies along the Himalayan foothills tend to correspond to positive anomalies along the Yangtze corridor and vice versa. In support of this claim, all-Asia JA EOF1 (+ over Himalayan foothills, + over Yangtze corridor) explains 9.4% of variance versus 5.2% explained by all-Asia JA EOF3 (+ over the Himalayan foothills, – over the Yangtze corridor). We create an AA_1 time series (China portion of all-Asia JA EOF1) by a linear combination of the C_1 and C_2 time series, and find a correlation with India temporal EOF1 of 0.46, which exceeds a 99.9% confidence level. We also repeat EOF analysis for the India and China subregions over different summertime periods: June–September and mei-yu season (mid-May–mid-July; 10-day bins). In each case, the resulting leading modes resemble India JA EOF1 and China JA EOFs 1 and 2 in Fig. 7. The fixity of leading regional modes throughout summer suggests that June all-Asia EOF1 and September all-Asia EOF1 are different from their July and August counterparts because of a change or absence of coupling between India and China. Finally, we test the effect of large domain size by applying varimax rotation to leading July–August all-Asia EOFs. The resulting leading mode resembles either India JA EOF1 or AA_1 ,

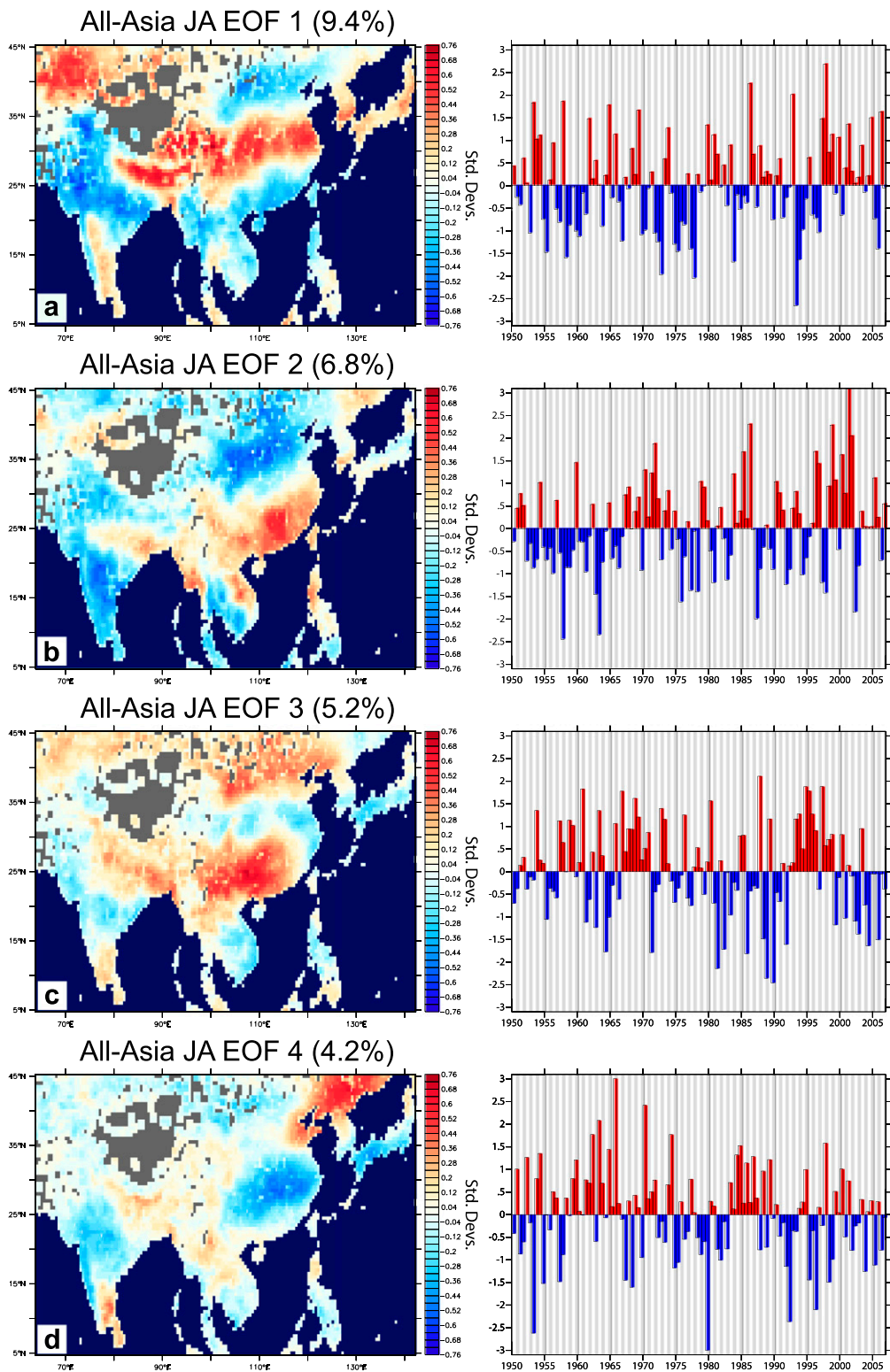


FIG. 6. Leading spatial and temporal EOFs of July–August normalized anomaly precipitation P'' for the all-Asia region (5° – 45° N, 64° – 142° E) with $0.5^{\circ} \times 0.5^{\circ}$ resolution for 1951–2007 (114 time points). Percentage of variance explained by each EOF is listed in parentheses. July (white shading) and August (gray shading) values of temporal EOF are shown separately. Time series are normalized to unit variance ($\sigma = 1$).

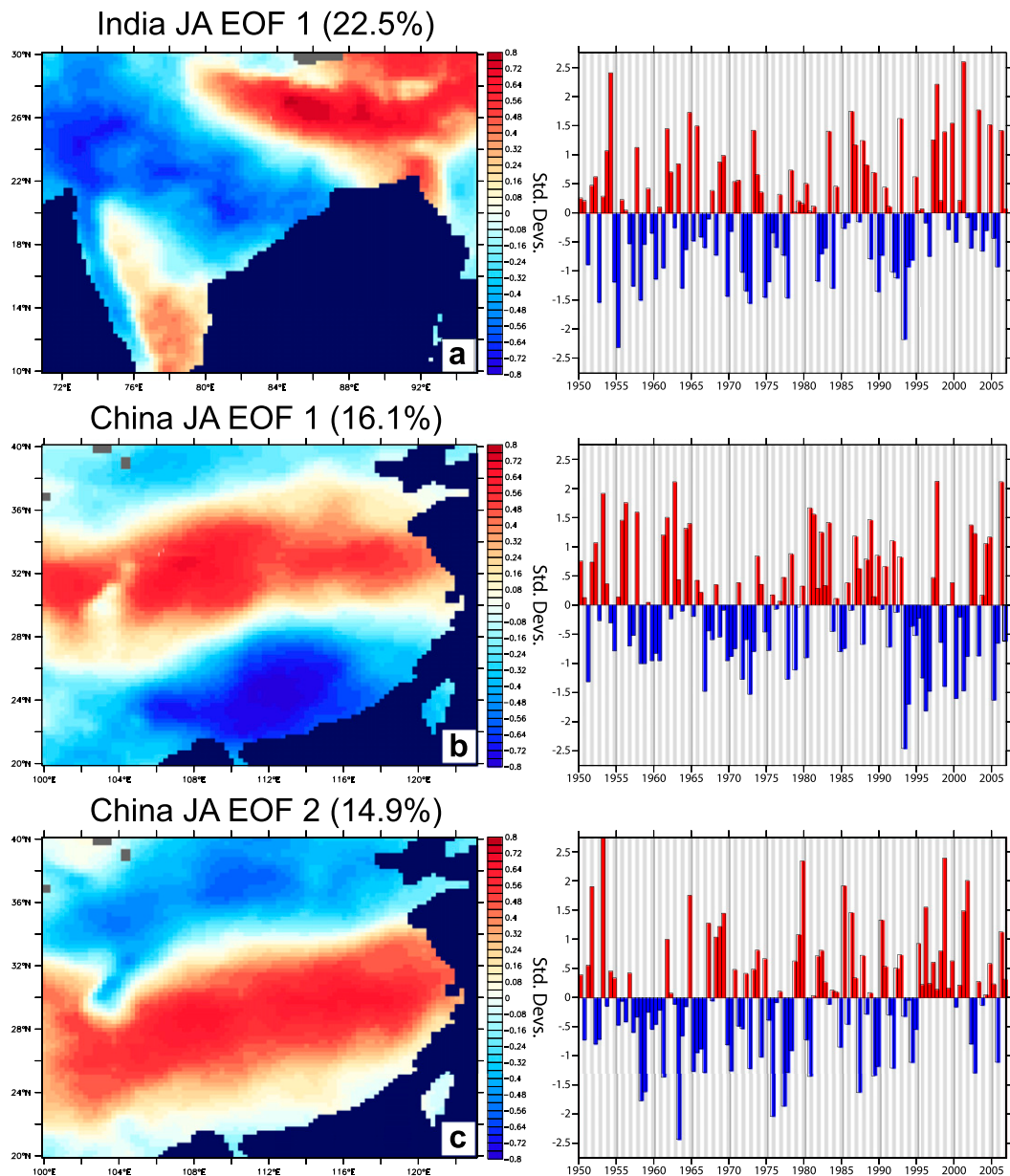


FIG. 7. Leading spatial and temporal EOFs of July–August normalized anomaly precipitation P'' for (a) India (10° – 30° N, 71° – 95° E) and (b), (c) China (20° – 40° N, 100° – 123° E) with $0.25^{\circ} \times 0.25^{\circ}$ resolution for 1951–2007 (114 time points). Percentage of variance explained by each EOF is listed in parentheses. July (white shading) and August (gray shading) are both shown. Time series are normalized to unit variance ($\sigma = 1$).

with no interregional coupling. However, this could reflect that the magnitude of regional variability within India or China is greater than that of the interregional signal.

In summary, the results of EOF analysis as shown in Figs. 5–7, in combination with the statistically significant point-to-point correlations and agreement map shown in Figs. 3 and 4, support the existence of a July–August coupling of rainfall anomalies between India and China.

5. Indices of all-Asia JA EOF1: All-Nepal rainfall and Yangtze rainfall

We seek an index of July–August all-Asia EOF1 that can be calculated using a smaller region. All-India monsoon rainfall (AIMR) has been used in many previous studies (Parthasarathy et al. 1994), and is made freely available by the Indian Meteorological Department (IMD; see acknowledgments for website), but the national boundaries

TABLE 2. July–August correlation coefficients r from 1951 to 2007 of all-Nepal rainfall, all-India rainfall (calculated from APHRODITE), monsoon zone (MZ) rainfall, and Yangtze (YZ) rainfall (mean rainfall over the region bounded by 29°N, 104.5°E; 32°N, 108°E; 34°N, 120°E; and 31.5°N, 122°E), as well as the oceanic Niño index (ONI) in preceding December [D(0), or equivalently the N(0)–D(0)–J(1) mean of Niño-3.4 (SST anomaly averaged over the region 5°S–5°N, 120°–170°W)]. Each time series is correlated with one another, as well as with all-Asia JA temporal EOF1, India JA temporal EOF1, China JA temporal EOFs 1 and 2, and official July–August all-India monsoon rainfall from the Indian Meteorological Department. Although all-Nepal monsoon rainfall is reliable only for 1961–2007 because of station coverage limitations and the monsoon zone time series likewise degrades after 1970, all 57 years are used for consistency, and results are not substantially affected. July and August are treated as separate time points except for correlation with ONI, which uses a single value per year. The 95% and 99% confidence levels are indicated by boldface font and asterisks, respectively, and are calculated to account for the shared autocorrelation between time series, which reduces the effective degrees of freedom (Livezey and Chen 1983).

| Index | All Nepal | All India | MZ | YZ | EOF1 (All Asia) | EOF1 (India) | EOF1/2 (China) | All India (IMD) |
|--------------|---------------|--------------|---------------|--------------|-----------------|---------------|----------------------|-----------------|
| All Nepal | 1* | −0.07 | −0.52* | 0.28* | 0.59* | 0.70* | 0.37*/0.14 | 0.02 |
| All India | −0.07 | 1* | 0.76* | −0.08 | −0.43* | −0.54* | −0.04/− 0.27* | 0.94* |
| Monsoon zone | −0.52* | 0.76* | 1* | −0.23 | −0.74* | −0.90* | −0.27*/−0.30* | 0.67* |
| Yangtze | 0.28* | −0.08 | −0.24 | 1* | 0.62* | 0.31* | 0.62*/0.61* | −0.11 |
| ONI | 0.11 | 0.26 | 0.15 | 0.15 | 0.10 | −0.02 | 0.17/−0.11 | 0.24 |

of India include subregions that are inversely correlated according to all-Asia JA EOF1 and India JA EOF1. Instead, we propose all-Nepal monsoon rainfall as a suitable index because of high positive amplitude of all-Asia JA EOF1 across the country and good station coverage from 1960 onward (Nepal borders shown in Fig. 1). In subsequent sections, we argue that this high amplitude results from Nepal’s sensitivity to changes in moisture transport from the Bay of Bengal. Previous authors have calculated all-Nepal monsoon rainfall time series (Kansakar et al. 2004), but the Nepal Department of Hydrology and Meteorology does not release such data publicly. APHRODITE contains a large subset of the 337 total precipitation stations in Nepal (number obtained from <http://dhm.gov.np>), and we have therefore compiled our own monthly time series (see Table S1 in the supplementary material).

As previously mentioned, July all-Asia EOF1 and August all-Asia EOF1 are very similar spatially. Furthermore, August all-Nepal rainfall is not significantly correlated with that in preceding July during 1951–2007 ($r = -0.14$), which implies that successive July and August monthly rainfall anomalies in Nepal are independent of one another. Therefore, we treat each July and August anomaly as a separate point in a joint July–August all-Nepal monsoon rainfall time series with 114 time points. Our index is expressed in units of standard deviation, with July rainfall anomalies normalized using July mean and variance and the equivalent procedure for August.

In China, the Yangtze corridor corresponds to a region of high AA₁ amplitude and AA₂ near zero. We define Yangtze rainfall as mean rainfall over the region bounded by the points 29°N, 104.5°E; 32°N, 108°E; 34°N, 120°E; and 31.5°N, 122°E that includes parts of Sichuan, Hubei, Anhui, and Jiangsu provinces (Fig. 1). We also compile a time series for the monsoon zone as defined in Gadgil (2003), also shown in Fig. 1. Each of these time

series is compiled for July–August using the same procedure described in the previous paragraph.

Table 2 shows the correlation of July–August all-Nepal monsoon rainfall and Yangtze rainfall with all-Asia JA EOF1 and other time series of interest, calculated using all Julys and Augusts from 1951 to 2007 (114 time points total). Wang and Gillies (2013) asserted that all-Nepal and all-India rainfall are uncorrelated, and thence claimed that Nepal rainfall undergoes a mode of decadal variability distinct from the rest of the South Asian monsoon. Instead, we find that all-Nepal monsoon rainfall matches India JA EOF1 closely, and is also significantly correlated with leading EOFs in China, even though its correlation with all-India monsoon rainfall is indeed near zero. The monsoon zone time series shows even better correspondence to leading EOF modes, but the number of stations within the region drops precipitously from over 3000 for 1951–70 to <800 beginning in 1971 due to delays in archiving data (Rajeevan et al. 2006). This leads us to prefer all-Nepal monsoon rainfall as an index of all-Asia JA EOF1. All-India monsoon rainfall remains strongly correlated with leading temporal EOFs because most of India lies in a region of negative all-Asia JA EOF1. However, all-India monsoon rainfall misses the connection to Yangtze monsoon rainfall that is revealed by the use of either all-Nepal monsoon rainfall or monsoon zone rainfall.

ENSO induces the leading mode of global interannual precipitation variability (Dai et al. 1997). Xie et al. (2009) showed that El Niño events, which peak in December, lead to robust changes in precipitation and atmospheric circulation in East Asia in the subsequent June to August through the Indian Ocean “capacitor effect.” We would like to determine whether all-Asia JA EOF1 reflects this process or some other mechanism. Therefore, we test the correlation of the oceanic Niño index (ONI) in preceding December with the other time

series in Table 2. ONI is a 3-month running mean of the Niño-3.4 time series [sea surface temperature (SST) anomalies averaged over the region 5°S–5°N, 120°–170°W]. SST measurements are derived from ERSST.v3b, identical to ERSST.v3 as described in Smith et al. (2008) but with satellite SST observations excluded because of known bias. This index matches that used in Xie et al. (2009). The baseline used to calculate anomalies by ONI is periodically adjusted to account for global increase in mean SST, but the difference in baseline between the 1950s and 2000s is only 0.3°C and does not influence results. ONI is correlated with all-India monsoon rainfall at a 95% confidence level, but not with any other time series. This suggests that all-Asia JA EOF1 is not a direct reflection of ENSO variability.

6. Storm tracks with APHRODITE

a. Previous work

In the search for a process that connects South and East Asia, we investigate the propagation of storms. A simple first hypothesis is that the patterns observed in Fig. 4 and all-Asia JA spatial EOF1 correspond to interannual changes in the frequency or trajectory of storms. Storms in the Asian monsoon can propagate across thousands of kilometers, but interface with topography in complex ways (Romatschke and Houze 2011). Luo et al. (2011) used *CloudSat* and *CALIPSO* satellite data to determine the horizontal and vertical length scales of storms in different regions (India, the Tibetan Plateau, and East Asia) and found that storms on the Tibetan Plateau are shallower and have a shorter horizontal length scale than storms in India. One possible interpretation of this result is that storms do not cross between India and the Tibetan Plateau. However, it has been known for decades that vortices on the Tibetan Plateau may, depending on synoptic conditions, propagate downstream to eastern China, where they induce heavy rainfall and potential flooding (Tao and Ding 1981; Murakami and Huang 1984; Chen and Dell’Osso 1984; Yasunari and Miwa 2006; Xu and Zipser 2011; Wang et al. 2012). Likewise, depressions from western Pacific tropical cyclones can cross Indochina and reach India from July to September depending on background circulation (Chen and Weng 1999; Fudeyasu et al. 2006). Thus, storms can propagate between South and East Asia under some circumstances. We quantify this behavior below.

b. Technique

Past studies have used the Hybrid Single Particle Lagrangian Integrated Trajectory (HYSPLIT) analysis to create back trajectories of air parcels in Asia during monsoon season (Medina et al. 2010; Cai et al. 2012; Gao

et al. 2013). However, HYSPLIT uses circulation obtained from reanalysis products, which struggle to produce realistic frequency distributions of precipitation in the region (Peña-Arancibia et al. 2013). As an alternative, we use lag–lead correlation with APHRODITE to extract the propagation of precipitation anomalies across days. This analysis cannot show all storms (e.g., storms that do not produce rainfall or that do not propagate across multiple days) but suffices to study the passage of storms between South and East Asia, which is our focus.

For a reference point i with normalized anomaly time series P_i'' and a phase lag of λ days, the lag–lead correlation $c_i^\lambda(x, y, \text{year})$ with rainfall at another point (x, y) is given by

$$c_i^\lambda(x, y, \text{year}) = \sum_{\text{days}} P_i''(\text{day}, \text{year}) P''(x, y, \text{day} + \lambda, \text{year}),$$

for $\lambda = -5, \dots, +5$ days and years 1950–2007.

This is identical to the formula for the correlation coefficient r with an offset of λ days between time series (a lag or lead depending on the sign of λ). APHRODITE cannot provide information on subdaily variation, propagation over oceans, or different mechanisms of propagation. However, the 57 years of data can be used to extract both mean storm trajectories and their interannual variability. The c_i^λ values require further processing to isolate propagation because there tends to be a nonzero positive background field independent of the value of λ . This background field, different for each reference point i , results from several effects, including the false positive correlation of two points without rain, even if they are distant from one another, and also the deviation of precipitation anomalies from a normal distribution. We define the background field $b_i(x, y)$ as the mean lag–lead correlation averaged over all λ and years, and thereafter analyze the anomaly from this background, $C_i^\lambda(x, y, \text{year})$, and the 57-yr mean anomaly $K_i^\lambda(x, y)$:

$$b_i(x, y) = \overline{c_i^\lambda(x, y, \text{year})}^{57 \text{ yr}, \lambda = -5, \dots, +5},$$

$$C_i^\lambda(x, y, \text{year}) = c_i^\lambda(x, y, \text{year}) - b_i(x, y), \quad \text{and}$$

$$K_i^\lambda(x, y) = \overline{C_i^\lambda(x, y, \text{year})}^{57 \text{ yr}}.$$

We calculate $C_i^\lambda(x, y, \text{year})$ and $K_i^\lambda(x, y)$ at every reference point for $\lambda = -5, \dots, 5$ and from 1951 to 2007. Figure 8 shows K_i^λ for reference points $i = 2, 6, 13, 16$, and 21 (Kathmandu, Durg, Shenzhen, Enshi, and Baotou) as well as two additional sites, Lijiang (26.9°N, 100.4°E) and Lake Qinghai (37.4°N, 100.1°E). In addition, for each reference point and lag λ , we find the

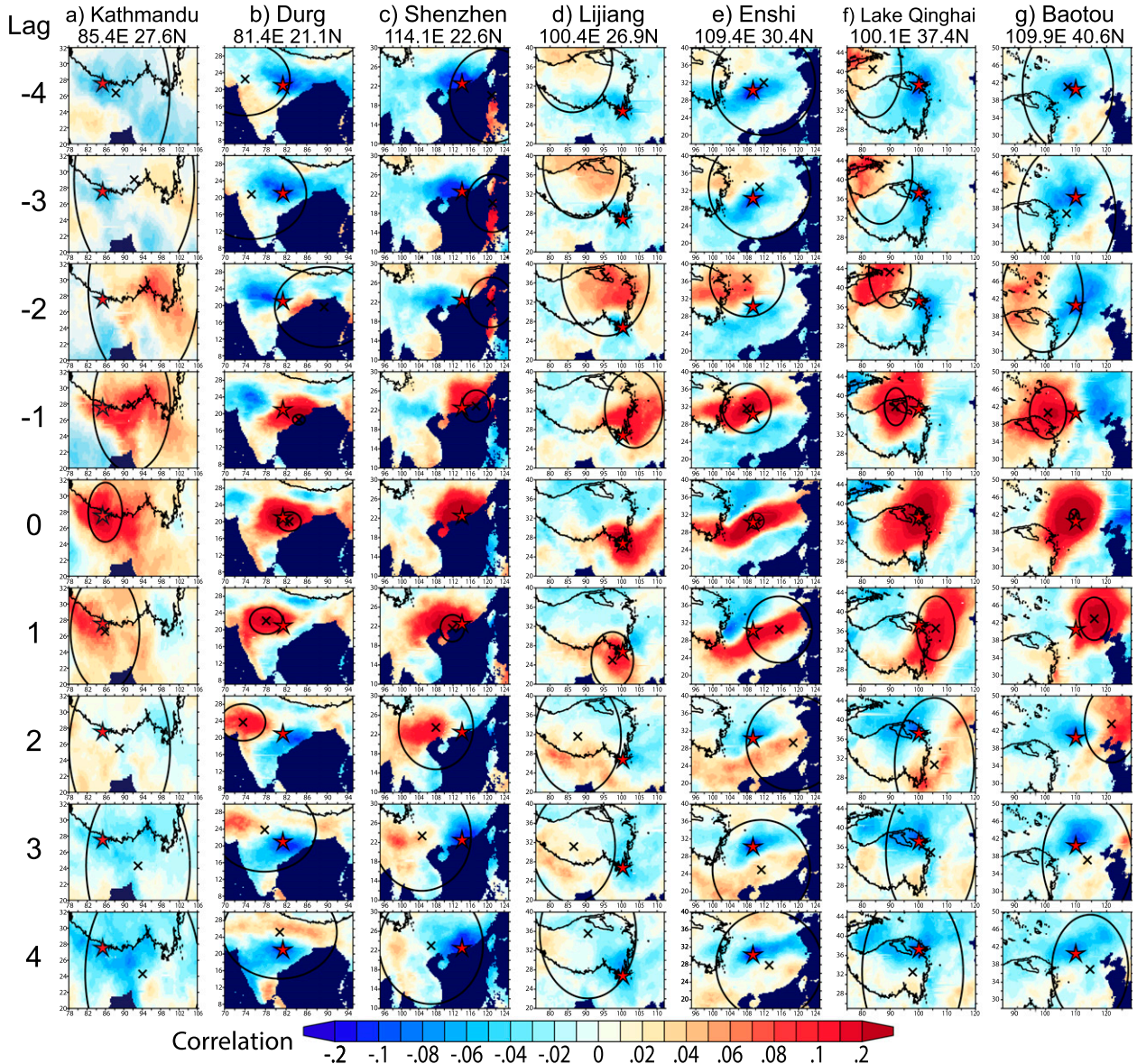


FIG. 8. July–August K_i^λ for reference point (x_i, y_i) (red star) and $\lambda = -4$ to 4, where K_i^λ is the 57-yr mean of anomalous correlation C_i^λ of local rainfall $P''(x_i, y_i)$ with normalized anomaly rainfall P'' at all other points, with an imposed lag or lead of λ days (see the main text for formula). Variance circles for a given λ are drawn to include at least 50% of yearly maxima of anomalous correlation C_i^λ from all 57 years, with the cross marking the center.

location of maximum $C_i^\lambda(x, y, \text{year})$ in each of the 57 years, and then draw the smallest circle that contains at least 50% of each of the yearly maxima. This quantifies interannual variability. Figure 9 condenses propagation information from Fig. 8 into a single composite image by showing the lag λ for which $K_i^\lambda(x, y)$ is maximized, with 50% variance circles for selected λ and connecting arrows superimposed. Using these tools, we focus on whether storms propagate between South and East Asia, whether storm tracks change between years, and what trajectories reveal about underlying dynamics.

c. Steering by 200-hPa-level winds

In Fig. 8, K_i^0 ($\lambda = 0$) reveals the size of storms at each reference point, typically around 300 km. Interannual variability is generally small for $\lambda = -2, \dots, 2$. Negative values of $K_i^\lambda(x, y)$ may result from a strong positive K_i^λ on another day, and should not necessarily be interpreted as storm suppression. All reference points show coherent propagation of anomalies across days.

We focus first on the South Asian monsoon domain. In the monsoon zone (Fig. 8b, Durg), storms propagate

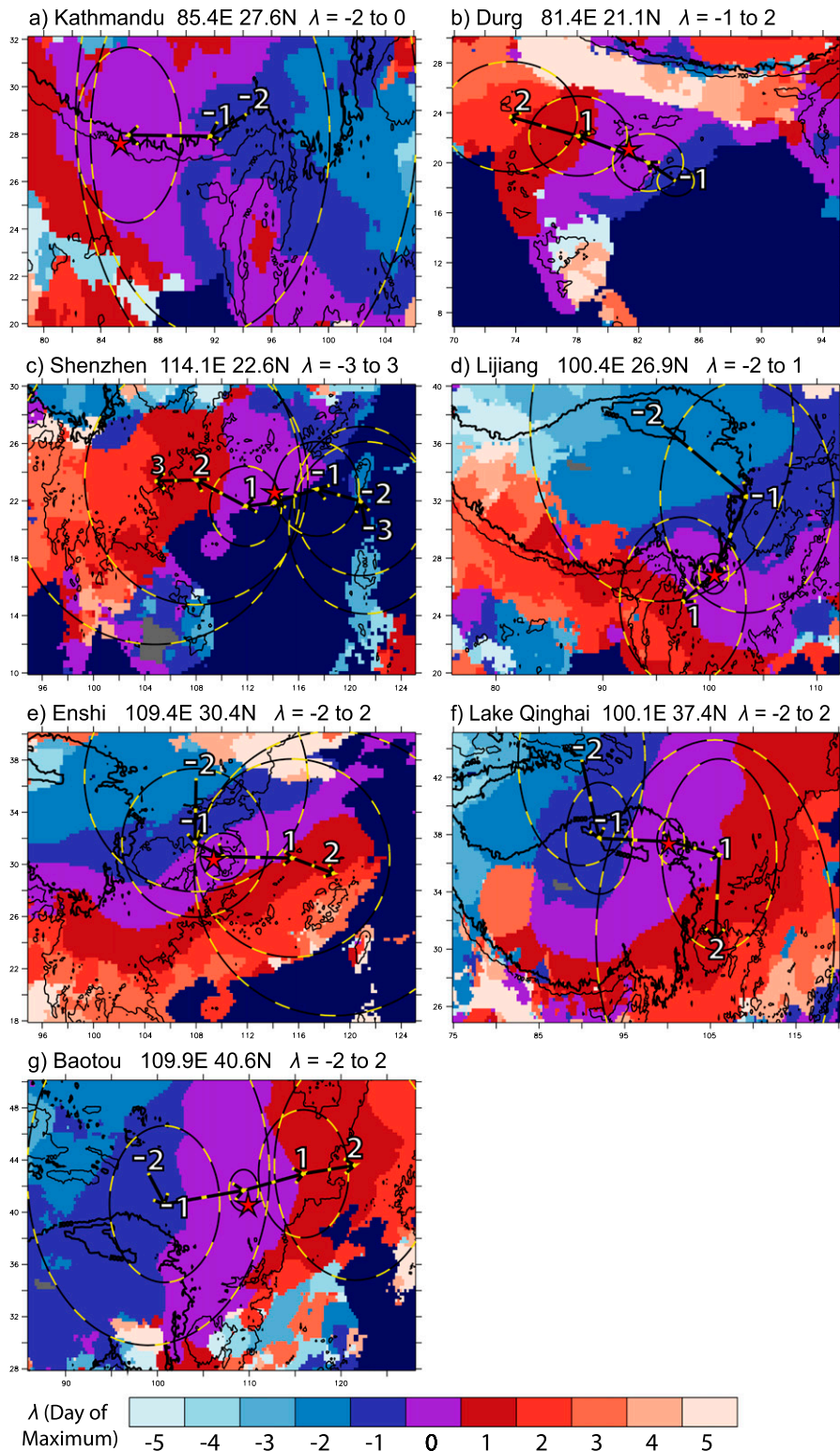


FIG. 9. July–August plot of the lag λ for which, given listed reference point (x_i, y_i) (red star), the 57-yr mean anomalous correlation of rainfall $K_i^\lambda(x, y)$ is maximized. Variance circles from Fig. 9 (black with yellow highlights) are superimposed for the range of λ listed above each figure, with connecting arrows showing propagation (also black with yellow highlights).

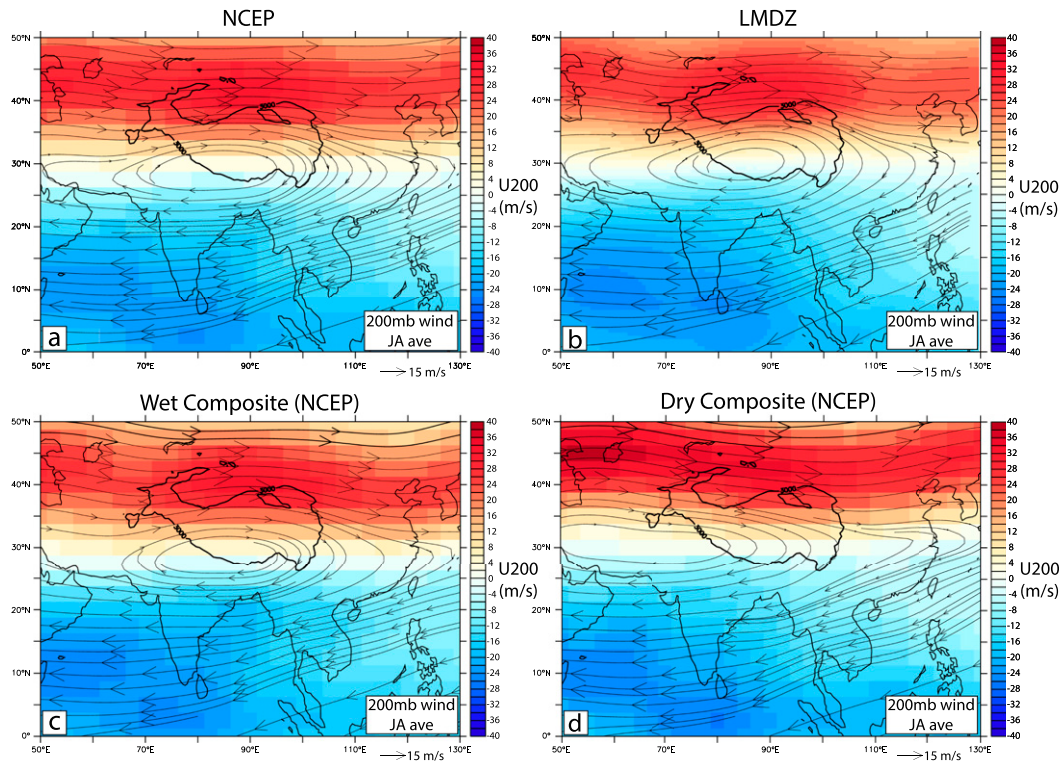


FIG. 10. July–August streamlines of (a) mean 200-hPa-level winds from NCEP reanalysis (1948–2014) and (b) LMDZ 200-hPa winds for 2006. NCEP reanalysis 200-hPa-level wind for composites of (c) “wet” and (d) “dry” years. The wet composite includes the five years with the most positive value of all-Asia JA EOF1, while the dry composite is the equivalent with the five most negative years.

west-northwestward from the Bay of Bengal with little variance in trajectory, also seen in past work such as Fig. 1 of Sikka (1977). These storms, known in the literature as “monsoon depressions” or “low pressure systems” (Sikka 1977; Chen and Weng 1999; Krishnamurthy and Ajayamohan 2010), generally do not reach tropical cyclone intensity. Instead, tropical cyclone occurrence in the Bay of Bengal is confined mostly to October–November and April–May (Li et al. 2013). Several previous studies show that monsoon depressions can originate from farther east over Indochina or the South China Sea (Saha et al. 1981). Storms reaching Kathmandu (Fig. 8a) also propagate westward, but their primary source is the Yunnan Plateau to the east, with a contribution from Bangladesh and the Bay of Bengal visible at $\lambda = -1$. In turn, Fig. 8d (Lijiang) shows that these Yunnan Plateau storms originate from the midlatitude westerlies north of the Tibetan Plateau ($\lambda = -5, \dots, -2$). Bay of Bengal depressions do not reach the Yunnan Plateau. The Himalayas divide regions of westerly and easterly propagation. Figures 8a and 8b also indicate that rainfall peaks over the Himalayan foothills and southern India 5 days before and after a storm passes through the monsoon zone, and vice versa. This reflects the spatial

pattern associated with intraseasonal oscillations (ISOs), an extensively studied 10–20-day mode of variability associated with the cycle of active and break periods in the South Asian monsoon (Krishnamurti and Ardanuy 1980; Chen and Chen 1993; Annamalai and Slingo 2001; Han et al. 2006; Fujinami et al. 2011, 2014).

In East Asia, the direction of propagation also shifts from westerly north of 30°N to easterly over South China. In Figs. 8c and 9c (Shenzhen), storms from the Philippines and Taiwan move northwestward to southern China and then westward toward the Yunnan Plateau, with low interannual variability for $\lambda = -2, \dots, 2$. This behavior has been seen both in observations (Chen and Weng 1999; Liu and Chan 2003) and in idealized monsoon studies (Privé and Plumb 2007b). Baotou, our northernmost reference point (Figs. 8g and 9g), sits at the July–August latitude of the tropospheric jet (Schiemann et al. 2009), and propagation is therefore strictly westerly. Central China marks the transition between westerly and easterly storm advection. Over Enshi (Figs. 8e and 9e; Yangtze corridor), westerly storms are sheared into northeast–southwest-tilted bands. This phenomenon, also seen in Figs. 8f and 9f (Lake Qinghai), can be understood by considering upper-level winds at this latitude (Fig. 10a).

If a midlatitude storm transported by the westerly jet is perturbed southward, it will gain westward velocity from mean flow, whereas storms passing farther to the north continue eastward. The Himalayas block the passage of storms between the Tibetan Plateau and India, but storms are able to traverse the lower terrain of the Yunnan Plateau.

In all regions, the direction of propagation agrees closely with 200-hPa-level winds (Fig. 10a). For the previously discussed monsoon depressions, this observation is in fact a coincidence. The west-northwestward travel of monsoon depressions instead results from an unusual secondary circulation that advects disturbances against lower-level flow without interacting with the upper troposphere (Chen and Yoon 2000; Chen et al. 2005), even though the predecessors of monsoon depressions are brought by upper-level winds from the east. In the rest of Asia, upper-level winds steer disturbances. We verify this claim by also performing lag-lead correlations for the months of June and September (not shown). Trajectories are mostly similar, and substantial changes correspond to changes in 200-hPa-level winds. The low interannual variability of storm trajectories results from the relative constancy of upper-level winds between years, as seen for instance with tropical cyclones in the western Pacific (Kumar and Krishnan 2005). The band of positive correlation in all-Asia JA EOF1 does not correspond to the storm tracks in Figs. 8 and 9 or to their interannual variations. Figures 10c and 10d show the 200-hPa-level winds associated with the five most positive EOF1 years (“wet” years) and five most negative years (“dry” years). The steering direction of storms remains steady in both, although some changes occur. A check of the K_i^λ in these wet and dry years also does not reveal major differences (not shown). Therefore, we propose that the interannual variability of storm trajectories does not explain the correlation of precipitation anomalies between South and East Asia.

d. An apparent contradiction

Storms are the proximate cause of precipitation, and yet Fig. 9 shows that July–August storm trajectories behave differently from monthly rainfall anomalies. Both respond to blocking by the Himalayas, but storm trajectories are less responsive to other low topography. The propagation direction of storms is roughly a function of latitude, without the local heterogeneity observed in rainfall. Last, the direction of storm tracks does not change much from year to year. Storms produce rainfall and yet appear incapable of explaining its variations on longer time scales.

A solution can be identified by considering northeastern India and the southeastern Tibetan Plateau.

Although Fig. 9d shows that storms in the region come from the Yunnan Plateau to the east, local observations of $\delta^{18}\text{O}$ show a Bay of Bengal origin and isotopic depletion from convection (Gao et al. 2011). The seeming incompatibility of storms and vapor history helps us to isolate two separate processes: storm propagation and moisture transport, both of which interact with mean flow in different ways. Storms are an eddy process superimposed on the mean state of the atmosphere. Synoptic depressions are steered by the upper troposphere and recycle whatever water vapor is locally available as they propagate. In contrast, because the scale height of water vapor is about 3 km, moisture transport depends on the state of the lower troposphere, where patterns of convergence change greatly from year to year (Annamalai and Slingo 2001; Yoon and Chen 2005). The fixity of storm trajectories points to changes in moisture transport as the root of interannual precipitation anomalies. In the next section, we propose a mechanism whereby such changes may induce coupling between South and East Asia.

7. Coupling between India and China

a. Proposed mechanism

We propose that years of anomalously heavy July–August rainfall over the Himalayan foothills reflect increased transport of water vapor from the Bay of Bengal. In turn, some of this surplus vapor travels via northeastern India to the southeastern Tibetan Plateau and northern Yunnan Plateau, and onward to the Yangtze corridor. In Sampe and Xie (2010), a linear baroclinic model (LBM) with prescribed heating over the Yangtze corridor produced a zonal band of ascent, as well as anomalous descent to the north and south (Figs. 13 and 14 of their paper). We suggest that increased latent heating associated with an increase in water vapor along the Yangtze corridor may supply a diabatic forcing similar to the Sampe and Xie experiment, and that the resulting vertical velocity anomalies could ultimately generate the tripole pattern of rainfall anomalies over China seen in all-Asia JA EOF1. In months with reduced moisture transport across the Yunnan Plateau, we therefore propose that the decrease in latent heating along the Yangtze corridor would lead to anomalous local descent and an inverted spatial pattern of rainfall anomalies. We further theorize that the coupling between India and China begins in July, when the onset of monsoon circulation in northern India initiates abundant moisture transport toward the Himalayas and onward to the Yunnan Plateau, and ends by September due to the shift of peak insolation back to the equator.

The strong dipole of Indian summer rainfall variability, and corresponding shift in moisture transport, may reflect the existence of two stable summer ITCZ positions over

India: an oceanic latitude at 5°N and a continental latitude at 15°N, as argued in [Gadgil \(2003\)](#). In turn, the preferred configuration of the ITCZ may be influenced by the state of ENSO and Indian Ocean SST. A full moisture budget equates the convergence of moisture transport with the balance of precipitation and evaporation ($P - E$) ([Trenberth 1991](#); [Chen and Bordoni 2014a](#)). For our purposes, we assume that an additional influx of moisture from the Bay of Bengal must translate to increased precipitation downstream. Also, our subsequent model results suggest that evaporation is a negligible component of the moisture budget during the monsoon.

b. Potential vorticity and moist static energy

The linkage of July–August rainfall anomalies in India and China can be understood in terms of conservation of potential vorticity (PV). The PV of a column of air is given by

$$\text{PV} \approx \frac{(\xi + f)}{H} = \text{constant},$$

where $\xi = \partial v/\partial x - \partial u/\partial y$ is the relative vorticity of the column, $f = 2\Omega \sin\phi$ is the planetary vorticity at latitude ϕ due to the rotation rate of Earth Ω , and H is the height of the column. This approximation is valid for a barotropic fluid. In this simple framework, heating acts by stretching a parcel and topography by compressing it. This helps to explain the sensitivity of flow even to low topography, and why moisture does not simply pass over the Arakan Mountains or Ghats.

A moisture parcel propagating northward from the Bay of Bengal cannot overcome the steep topography gradient of the Himalayas (which sharply decreases H). Instead, trajectories bifurcate between a westward branch toward Nepal ($\xi > 0$) and eastward forced channel flow between the Himalayas and Arakan Mountains into northeastern India ($\xi < 0$). These two trajectories encounter different topography. To the west, the Himalayas exceed 5 km of altitude, preventing access of moisture to the quasi-desertic western Tibetan Plateau. To the east, the Himalayas are slightly lower, the slopes are less steep, and river valleys allow access to the high terrain of the eastern Tibetan Plateau and Yunnan Plateau. During monsoon season, moisture is observed to propagate as far as Lhasa and up the Brahmaputra and Zayu river valleys, which run from the Tibetan Plateau's southeastern edge into northeastern India ([Gao et al. 2011](#); [Yang et al. 2012](#)). Propagation may also be aided by the phenomenon described in [Holton \(2004, 86–115\)](#), namely that perturbations in easterly flow are damped whereas westerly flow excursions are amplified because of the gradient of planetary vorticity. Last, moist flow upslope may be abetted by

surface heating, which should lift isentropes ([Molnar and Emanuel 1999](#); [Privé and Plumb 2007b](#)).

In practice, we lack information about individual parcels. Instead, moist static energy h , and in particular the subcloud quantity h_b , reveals information about the strength and extent of the monsoon ([Privé and Plumb 2007a,b](#)). Note that h tracks total potential energy per kilogram of air (units of J kg^{-1} or $\text{m}^2 \text{s}^{-2}$), including latent heating, sensible heating, and potential energy:

$$h = L_v q + c_p T + gz,$$

where L_v is the latent heat of vaporization of water, q is the specific humidity, c_p is the specific heat of dry air, T is temperature, g is the acceleration due to gravity, and z is altitude. In the absence of diabatic heating, this quantity remains conserved. Following [Boos and Kuang \(2010\)](#), h is expressed in units of kelvin by dividing by c_p . The resulting quantity can be interpreted as the equivalent temperature the parcel would have at sea level if all moisture were condensed. According to both idealized studies and observation, the maximum of h_b occurs at the northernmost extent of monsoon circulation ([Emanuel 1995](#); [Privé and Plumb 2007a](#); [Boos and Kuang 2010](#); [Nie et al. 2010](#)). Therefore, if our hypothesis of abundant moisture transport from the Bay of Bengal to northeastern India and onward is correct, we should observe an associated h_b maximum there that also diffuses downstream onto the southern Tibetan Plateau, northern Yunnan Plateau, and beyond. The Himalayas amplify the h_b maximum along the Himalayan foothills both by shielding warm air over India from cold air farther north ([Boos and Kuang 2010](#)) and by forced wind and moisture convergence. The Arakan Mountains may further induce convergence and strengthen h_b by restricting atmospheric flow into northeastern India to a narrow channel.

c. Supporting evidence

APHRODITE shows that northeastern India experiences intense summer rainfall of 20–30 mm day⁻¹ ([Fig. 1](#)). Such rates require substantial moisture advection inland. Several past studies demonstrate this transport. As previously mentioned in [sections 3b](#) and [6d](#), studies of $\delta^{18}\text{O}$ of precipitation on the southeastern Tibetan Plateau suggest a Bay of Bengal origin ([Yao et al. 2009](#); [Gao et al. 2011](#); [Yang et al. 2012](#)). [Zhang et al. \(2013\)](#), using Atmospheric Infrared Sounder (AIRS) satellite retrievals corroborated by radiosonde observations, find a deep layer of water vapor on the Tibetan Plateau in summer, with up to 15 mm of precipitable water over the southeastern Tibetan Plateau and northern Yunnan Plateau. In [Medina et al. \(2010\)](#), analysis of TRMM satellite data shows massive stratiform storms that advect moisture from the Bay of

Bengal and wetlands of Bangladesh to the eastern Himalayas. Tagging of water in isotope-enabled GCM runs with the LMDZ model (which we use in the next section) show some transport of Bay of Bengal water vapor to central and southern China (Yao et al. 2013).

Direct observations of water vapor transport are unavailable. Several previous studies have suggested that changes in moisture transport over India induce precipitation anomalies in China (Feng and Zhou 2012; Cao et al. 2014), but the resolution of the reanalysis products used in these studies ($2.5^\circ \times 2.5^\circ$ and $1.25^\circ \times 1.25^\circ$ resolution, respectively) may be unable to produce realistic fields of moisture transport. Pausata et al. (2011) argued that, during Heinrich events, East Asian speleothems record decreased Indian monsoon rainfall due to the downstream advection of isotopically enriched water vapor. However, their proposed pathway is farther south over Indochina and does not correspond to all-Asia JA EOF1.

The covariation of precipitation anomalies in South and East Asia does not require a direct link, since each region could be independently responding to the same external forcing. Nonetheless, we propose a pathway of moisture transport from India to China across the Yunnan Plateau as a simple mechanism whose variations can explain our results. In the following section, we test our hypothesis by analyzing results from a model with high resolution around the Tibetan Plateau.

8. Model results

a. Specifications

We employ the LMDZ model, version 5 (LMDZ5), to investigate the proposed mechanism, specifically the LMDZ5A package used in phase 5 of the Coupled Model Intercomparison Project (CMIP5) as part of the Intergovernmental Panel on Climate Change Fifth Assessment Report (IPCC AR5; Christensen et al. 2011). LMDZ is the flagship atmospheric model of the Institute Pierre-Simon Laplace (IPSL). Details of model function are available in Hourdin et al. (2006) and Hourdin et al. (2013). The run analyzed below uses the AMIP protocol, which fixes CO_2 and prescribes monthly fields of SST and sea ice with some interannual variability. A high-resolution nested grid (~ 50 -km resolution) is included over East Asia (0° – 55°N , 60° – 130°E) inside of a coarse global grid. The transition from coarse to fine resolution occurs over an area far outside of the region of interest in order to avoid edge effects. In addition, winds are nudged towards the ECMWF reanalysis data with a dissipation time constant τ of 1 or 4 h (inside or outside zoomed region, respectively).

The combination of zoomed grid and nudged winds substantially improves precipitation and $\delta^{18}\text{O}$ climatologies

relative to observation (Gao et al. 2011). An isotope-enabled version of LMDZ (LMDZ-iso) has been tested across a range of climates with good performance (Risi et al. 2010). LMDZ has also been extensively tested in the vicinity of the Tibetan Plateau and consistently outperforms other isotopically enabled models (Gao et al. 2011; Lee et al. 2012; Eagle et al. 2013; Gao et al. 2013; Yao et al. 2013). We present results for 2006 as a case study, leaving in-depth testing and investigation of interannual variability for future runs. Rainfall climatology roughly resembles observations from APHRODITE, with correct seasonality over South and East Asia (not shown). Figure 10b shows that LMDZ produces a field of 200-hPa-level wind similar to NCEP reanalysis (Fig. 10a).

b. Moist static energy and moisture transport in LMDZ

To analyze model treatment of the South Asian monsoon, we calculate near-surface moist static energy h_b , and also streamlines of column-integrated moisture transport $\mathbf{Q} = (Q_u, Q_v)$ for each month from June to September (Fig. 11), where $Q_u = 1/g \int qu dp$ and $Q_v = 1/g \int qv dp$ (Trenberth 1991). The direction of \mathbf{Q} is mostly dictated by circulation in the lower troposphere, where specific humidity is much higher. Our calculated values agree with past estimates such as in Feng and Zhou (2012).

LMDZ's estimate of h_b can be compared to the July climatology of 10-m moist static energy in Fig. 1 of Nie et al. (2010) and Fig. 3a of Boos and Hurley (2013), which it mostly resembles. In July and August, LMDZ correctly generates a maximum of moist static energy along the Himalayan foothills and east of the Hindu Kush, a feature absent from almost all CMIP5 GCMs (Boos and Hurley 2013). This maximum is due to the abundant advection of moisture from the Bay of Bengal by cyclonic mean circulation. In June, the h_b maximum is instead situated over the Arabian Ocean and Bay of Bengal because winds over India are westerly, which brings dry air from the continental interior. Bay of Bengal SSTs also peak in May and June according to observations (Bhat et al. 2004). In September, h_b is lower everywhere because of decreased insolation, although cyclonic circulation and northward moisture transport from the Bay of Bengal persist in weakened form. Over the northern Bay of Bengal, peak column-integrated moisture transport across 22°N onto land is $314.5 \text{ kg m}^{-1} \text{ s}^{-1}$ in July, $262.8 \text{ kg m}^{-1} \text{ s}^{-1}$ in August, and $206.9 \text{ kg m}^{-1} \text{ s}^{-1}$ in September. This agrees with the observation that water vapor from the Bay of Bengal still reaches Lhasa in September, but less frequently than in July and August (Gao et al. 2011). Abundant moisture transport from the Bay of Bengal to the Himalayan foothills requires cyclonic circulation over

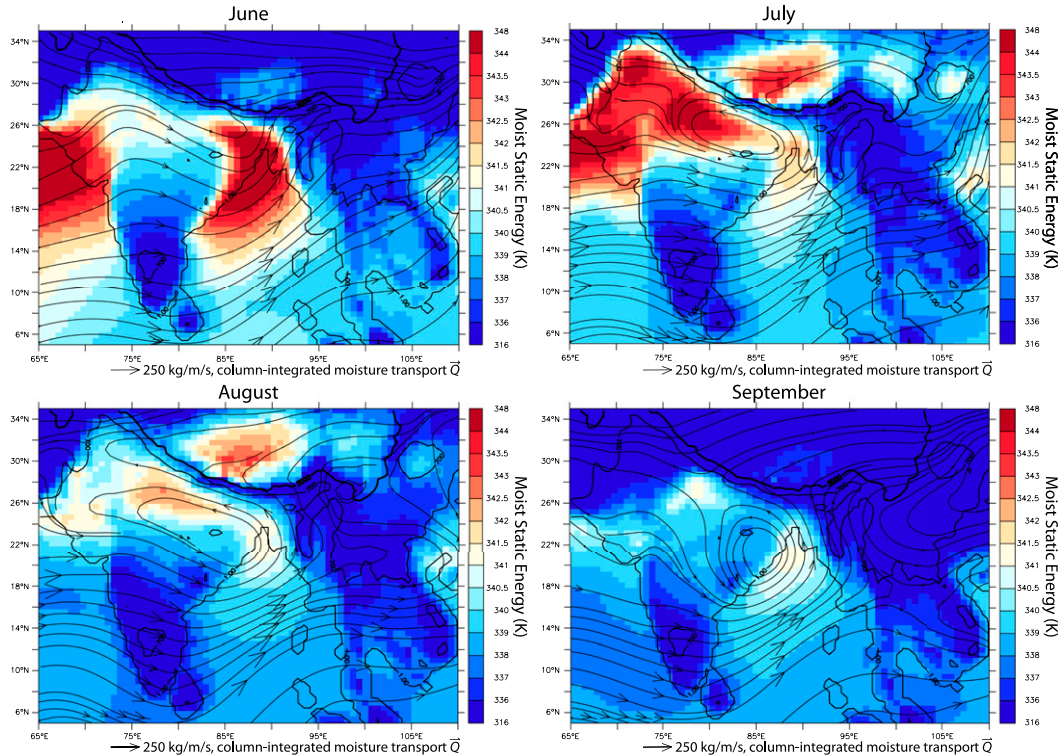


FIG. 11. LMDZ values of near-surface moist static energy h_b (shading) and column-integrated moisture transport \bar{Q} (streamlines, magnitude shown by size of arrowheads) for each month from June to September 2006 over the region 5° – 35° N, 65° – 110° E. Moist static energy is given by the formula $h_b = c_p T + L_v q + gz$, with variables defined in the main text. Units of moist static energy are in kelvin, obtained by dividing h_b by c_p as practiced in [Boos and Hurley \(2013\)](#). Column-integrated moisture transport is given by $\bar{Q} = 1/g \int q u dp$. Note the unusual color scale of moist static energy used to emphasize changes over continental India.

India and sufficient heating. In this run, these conditions are only met in July and August.

LMDZ also shows moisture transport from India downstream to China in July and August, and corresponding local maxima in moist static energy over the southeastern Tibetan Plateau and Sichuan basin. In the model, there is a positive bias in moist static energy and rainfall over the central Tibetan Plateau relative to observation. Meanwhile, in northeastern India, moist static energy is underestimated by 20–25 K, and rainfall by 20 mm day^{-1} . Therefore, we suggest that the route of moisture transport from the Bay of Bengal to the Yangtze corridor is shifted northward in LMDZ by about 5° of latitude, and that the actual route is through northeastern India and across the Yunnan Plateau.

9. Conclusions

In this work we find that July–August monthly rainfall anomalies in South and East Asia are correlated across thousands of kilometers as shown by point-to-point correlations, an agreement map method, and EOF analysis.

Further investigation with lag–lead correlations of rainfall shows that interannual variations in storm tracks cannot explain this result. Instead, we postulate that a pathway of moisture transport exists from the Bay of Bengal to the Yangtze corridor across the northern Yunnan Plateau. Changes in this transport produce a coherent band of rainfall anomalies connecting northeastern India and central China, and also induce changes of opposite sign in the monsoon zone, northern China, and southern China. This link is confined to July and August, when cyclonic monsoon circulation sets in over India and insolation remains high. We propose all-Nepal and Yangtze monsoon rainfall as two local indices that reflect this leading mode of Asian rainfall variability. The LMDZ model, featuring a high-resolution grid around the Tibetan Plateau, produces a realistic monsoon climatology and confirms basic elements of our hypothesis, which offers promise for future modeling efforts.

It is important to understand the role of storms. On a daily time scale, the passage of a storm induces a positive rainfall anomaly. They also alter their synoptic environment by processes such as the release of CAPE,

such that storms and atmospheric conditions evolve in tandem. Yet, at the monthly level, our results suggest that the leading mode of July–August rainfall variability in Asia cannot be attributed to a change in storm behavior. Storms function as a passive, stochastic process that registers the state of the atmosphere by precipitating available water vapor. Since the scale height of water vapor is about 3 km, lower tropospheric conditions dictate its distribution. Increased moisture transport to the Himalayas requires corresponding changes in circulation, lower-level convergence, and the distribution of near-surface moist static energy, which is correlated with seasonal rainfall anomalies in monsoon regions (Hurley and Boos 2013). In contrast, the steering direction of storms remains relatively constant between years. The agreement of storm tracks with 200-hPa-level winds suggests that their propagation across Asia is generally an upper tropospheric process, with some regional exceptions. Therefore, they are insensitive to orography besides the high barrier of the Himalayas. The sharp spatial gradients of rainfall and monthly rainfall anomalies reflect sensitivity to lower tropospheric processes, where topography dictates flow.

The lack of observations along the proposed route of moisture transport hinders the corroboration of our theory. Many locations traversed are remote or politically sensitive, such as the eastern Tibetan Plateau in China, Arunachal Pradesh in India, or Kachin state in Myanmar. Meteorological data alone may be insufficient to characterize the behavior of water vapor. Studies have compiled event-based measurements of isotopes at downstream sites in China (Yang et al. 2011; Wu et al. 2015), but the complexity of their $\delta^{18}\text{O}$ signals makes interpretation of parcel origin and history a challenge. An ideal study would feature daily or sub-daily measurement of water vapor at multiple sites en route, including northeastern India, the Yunnan Plateau, and Sichuan, similar to measurements performed at several sites along the Brahmaputra River valley on the Tibetan Plateau by Gao et al. (2011).

We note an additional connection between Bay of Bengal sea surface temperature (SST) and Indian rainfall variability. Using Hadley Centre SST dataset, version 3.1 (HadSST3.1; Kennedy et al. 2011a,b), which features SST from 1850 to present on a $5^\circ \times 5^\circ$ grid, we test the correlation of July–August rainfall in India at every point with SST in the northern Bay of Bengal (defined as the mean of SST at 22.5°N , 87.5°E and at 22.5°N , 92.5°E). The resulting pattern again resembles all-Asia JA spatial EOF1 (not shown), with positive correlations over the Himalayan foothills, eastern Tibetan Plateau, and Yangtze corridor and negative correlation over the monsoon zone, all exceeding a 95%

confidence level ($|r| > 0.18$). However, the time series of northern Bay of Bengal SST is not significantly correlated with all-Asia JA temporal EOF1 ($r = 0.11$) or India temporal EOF1 ($r = 0.09$). This result is robust to different definitions of Bay of Bengal SST. Indian monsoon rainfall variability and Bay of Bengal SST have previously been shown to covary on weekly time scales (Vecchi and Harrison 2002; Han et al. 2006). The covariance of local SST and monthly rainfall anomalies implies a mutual response to external forcing that we will investigate in future work.

The results above have only briefly considered the source of the coupled variability described above. Previous work has shown the ability of El Niño conditions in the central Pacific to induce droughts over India in following summer (Kumar et al. 2006), as well as circulation and rainfall anomalies over East Asia via the “capacitor effect” (Xie et al. 2009). We found no significant correlation between the Niño-3.4 index (ONI) in December and the leading July–August modes of South and East Asian rainfall variability (all-Asia JA EOF1, India JA EOF1, and China JA EOFs 1 and 2; correlations shown in Table 2). However, the correlation of December Niño-3.4 and all-India monsoon rainfall exceeds a 95% confidence level, suggesting that ENSO-related anomalies may have a particular spatial character distinct from India EOF1. Both equatorial Indian Ocean zonal wind and SST anomalies have been linked to variations in rainfall over India (Ihara et al. 2007; Mishra et al. 2012). Thus, leading modes of global and regional variability such as the western Pacific anticyclone (Kosaka et al. 2011), the Pacific decadal oscillation (Mantua and Hare 2002), and the Indian Ocean dipole (Saji et al. 1999) may influence the Indian monsoon by altering circulation or SSTs. However, the atmospheric response is sensitive to the exact distribution of such anomalies (Xie et al. 2009).

Statistically significant twentieth-century trends in rainfall have been found across Asia (Christensen et al. 2011; Singh et al. 2014). The leading temporal EOFs in our study (Figs. 6 and 7) generally show that precipitation has increased along the Himalayan foothills and China south of 30°N (Hunan and Jiangxi provinces in particular), and decreased over the monsoon zone and in northern China around 35°N (particularly Shaanxi and Henan provinces). This agrees with previous studies that discuss a “south flood–north drought” pattern in China (Ding et al. 2008) and a decrease in all-India monsoon rainfall since the 1970s (Annamalai et al. 2013). These results could reflect a change in mean moisture transport from the Bay of Bengal to China in the past few decades. A better physical understanding of the coupling between the South and East Asian monsoons may improve

projections of twenty-first-century precipitation changes in Asia, which remain uncertain (Christensen et al. 2011).

Acknowledgments. This work was supported by NSF funds EAR-0909195 and EAR-1211925. We also acknowledge NSFC (National Natural Science Foundation of China) Grant 40921120406 for encouraging the feedback and support of colleagues in China. We thank Jinqiang Chen, Peter Molnar, and two anonymous reviewers for their valuable suggestions. APHRODITE precipitation data are publicly available at <http://www.chikyu.ac.jp/precip/index.html>. Ferret, a NOAA product, was used for data analysis and preliminary plot generation. The official all-India monsoon rainfall time series was obtained from the Indian Meteorological Department (IMD) website at http://www.imd.gov.in/section/nhad/dynamic/Monsoon_frame.htm. The oceanic Niño index (ONI) time series was retrieved from NOAA at http://www.cpc.ncep.noaa.gov/products/analysis_monitoring/ensostuff/ensoyears.shtml. Monthly 200-hPa-level reanalysis winds were obtained from NCEP–NCAR reanalysis available at <http://www.esrl.noaa.gov/psd/data/gridded/data.ncep.reanalysis.derived.surface.html>. Bay of Bengal SST was obtained from HadSST 3.1, provided by the UK Met Office at <http://www.metoffice.gov.uk/hadobs/hadst3/data/download.html>. Data, figures used, and animations of relevant data are available online at <http://www.atmos.berkeley.edu/~jessed/myfigures.html>.

REFERENCES

- Aksoy, H., 2000: Use of gamma distribution in hydrological analysis. *Turk. J. Eng. Environ. Sci.*, **24**, 419–428.
- Annamalai, H., and J. Slingo, 2001: Active/break cycles: Diagnosis of the intraseasonal variability of the Asian summer monsoon. *Climate Dyn.*, **18**, 85–102, doi:10.1007/s003820100161.
- , J. Hafner, K. P. Sooraj, and P. Pillai, 2013: Global warming shifts the monsoon circulation, drying South Asia. *J. Climate*, **26**, 2701–2718, doi:10.1175/JCLI-D-12-00208.1.
- Barnes, E., and D. Hartmann, 2012: The global distribution of atmospheric eddy length scales. *J. Climate*, **25**, 3409–3416, doi:10.1175/JCLI-D-11-00331.1.
- Bhat, G. S., G. A. Vecchi, and S. Gadgil, 2004: Sea surface temperature of the Bay of Bengal derived from the TRMM Microwave Imager. *J. Atmos. Oceanic Technol.*, **21**, 1283–1290, doi:10.1175/1520-0426(2004)021<1283:SSTOTB>2.0.CO;2.
- Biasutti, M., S. E. Yuter, C. D. Burleyson, and A. H. Sobel, 2012: Very high resolution rainfall patterns measured by TRMM precipitation radar: Seasonal and diurnal cycles. *Climate Dyn.*, **39**, 239–258, doi:10.1007/s00382-011-1146-6.
- Boos, W. R., and Z. Kuang, 2010: Dominant control of the South Asian monsoon by orographic insulation versus plateau heating. *Nature*, **463**, 218–222, doi:10.1038/nature08707.
- , and J. V. Hurlley, 2013: Thermodynamic bias in the multi-model mean boreal summer monsoon. *J. Climate*, **26**, 2279–2287, doi:10.1175/JCLI-D-12-00493.1.
- , and Z. Kuang, 2013: Sensitivity of the South Asian monsoon to elevated and non-elevated heating. *Sci. Rep.*, **3**, 1192, doi:10.1038/srep01192.
- Bordoni, S., and T. Schneider, 2008: Monsoons as eddy-mediated regime transitions of the tropical overturning circulation. *Nat. Geosci.*, **1**, 515–519, doi:10.1038/ngeo248.
- Cai, Y., and Coauthors, 2012: The Holocene Indian monsoon variability over the southern Tibetan Plateau and its teleconnections. *Earth Planet. Sci. Lett.*, **335–336**, 135–144, doi:10.1016/j.epsl.2012.04.035.
- Cao, J., P. Yao, L. Wang, and K. Liu, 2014: Summer rainfall variability in low-latitude highlands of China and subtropical Indian Ocean dipole. *J. Climate*, **27**, 880–892, doi:10.1175/JCLI-D-13-00121.1.
- Chelton, D., and R. Davis, 1982: Monthly mean sea-level variability along the west coast of North America. *J. Phys. Oceanogr.*, **12**, 757–784, doi:10.1175/1520-0485(1982)012<0757:MMSLVA>2.0.CO;2.
- Chen, J., and S. Bordoni, 2014a: Intermodel spread of East Asian summer monsoon simulations in CMIP5. *Geophys. Res. Lett.*, **41**, 1314–1321, doi:10.1002/2013GL058981.
- , and —, 2014b: Orographic effects of the Tibetan Plateau on the East Asian summer monsoon: An energetic perspective. *J. Climate*, **27**, 3052–3072, doi:10.1175/JCLI-D-13-00479.1.
- Chen, S.-J., and L. Dell’Osso, 1984: Numerical prediction of the heavy rainfall vortex over eastern Asia monsoon region. *J. Meteor. Soc. Japan*, **62**, 730–747.
- Chen, T.-C., and J.-M. Chen, 1993: The 10–20-day mode of the 1979 Indian monsoon: Its relation with the time variation of monsoon rainfall. *Mon. Wea. Rev.*, **121**, 2465–2482, doi:10.1175/1520-0493(1993)121<2465:TDMOTI>2.0.CO;2.
- , and S.-P. Weng, 1999: Interannual and intraseasonal variations in monsoon depressions and their westward-propagating predecessors. *Mon. Wea. Rev.*, **127**, 1005–1020, doi:10.1175/1520-0493(1999)127<1005:IAIVIM>2.0.CO;2.
- , and J.-H. Yoon, 2000: Some remarks on the westward propagation of the monsoon depression. *Tellus*, **52A**, 487–499, doi:10.1034/j.1600-0870.2000.01127.x.
- , —, and S.-Y. Wang, 2005: Westward propagation of the Indian monsoon depression. *Tellus*, **57A**, 758–769, doi:10.1111/j.1600-0870.2005.00140.x.
- Christensen, J. H., and Coauthors, 2011: Climate phenomena and their relevance for future regional climate change. *Climate Change 2013: The Physical Science Basis*, T. F. Stocker et al., Eds., Cambridge University Press, 1217–1308.
- Dai, A., I. Y. Fung, and A. D. Del Genio, 1997: Surface observed global land precipitation variations during 1900–88. *J. Climate*, **10**, 2943–2962, doi:10.1175/1520-0442(1997)010<2943:SOGLPV>2.0.CO;2.
- Ding, Y., and J. C. L. Chan, 2005: The East Asian summer monsoon: An overview. *Meteor. Atmos. Phys.*, **89**, 117–142, doi:10.1007/s00703-005-0125-z.
- , Z. Wang, and Y. Sun, 2008: Inter-decadal variation of the summer precipitation in East China and its association with decreasing Asian summer monsoon. Part I: Observed evidences. *Int. J. Climatol.*, **28**, 1139–1161, doi:10.1002/joc.1615.
- Eagle, R. A., C. Risi, J. L. Mitchell, J. M. Eiler, U. Seibt, J. D. Neelin, G. Li, and A. K. Tripathi, 2013: High regional climate sensitivity over continental China constrained by glacial-recent changes in temperature and the hydrological cycle. *Proc. Natl. Acad. Sci. USA*, **110**, 8813–8818, doi:10.1073/pnas.1213366110.
- Emanuel, K., 1995: On thermally direct circulations in moist atmospheres. *J. Atmos. Sci.*, **52**, 1529–1534, doi:10.1175/1520-0469(1995)052<1529:OTDCIM>2.0.CO;2.

- Feng, L., and T. Zhou, 2012: Water vapor transport for summer precipitation over the Tibetan Plateau: Multidata set analysis. *J. Geophys. Res.*, **117**, D20114, doi:10.1029/2011JD017012.
- Fudeyasu, H., S. Iizuka, and T. Matsuura, 2006: Seasonality of westward-propagating disturbances over Southeast and South Asia originated from typhoons. *Geophys. Res. Lett.*, **33**, L10809, doi:10.1029/2005GL025380.
- Fujinami, H., and Coauthors, 2011: Characteristic intraseasonal oscillation of rainfall and its effect on interannual variability over Bangladesh during boreal summer. *Int. J. Climatol.*, **31**, 1192–1204, doi:10.1002/joc.2146.
- , T. Yasunari, and A. Morimoto, 2014: Dynamics of distinct intraseasonal oscillation in summer monsoon rainfall over the Meghalaya–Bangladesh–western Myanmar region: Covariability between the tropics and mid-latitudes. *Climate Dyn.*, **43**, 2147–2166, doi:10.1007/s00382-013-2040-1.
- Gadgil, S., 2003: The Indian monsoon and its variability. *Annu. Rev. Earth Planet. Sci.*, **31**, 429–467, doi:10.1146/annurev.earth.31.100901.141251.
- , and S. Gadgil, 2006: The Indian monsoon, GDP and agriculture. *Econ. Polit. Wkly.*, **41**, 4887–4895.
- Gao, J., V. Masson-Delmotte, T. Yao, L. Tian, C. Risi, and G. Hoffmann, 2011: Precipitation water stable isotopes in the south Tibetan Plateau: Observations and modeling. *J. Climate*, **24**, 3161–3178, doi:10.1175/2010JCLI3736.1.
- , —, C. Risi, Y. He, and T. Yao, 2013: What controls precipitation $\delta^{18}\text{O}$ in the southern Tibetan Plateau at seasonal and intra-seasonal scales? A case study at Lhasa and Nyalam. *Tellus*, **65B**, 21043, <http://dx.doi.org/10.3402/tellusb.v65i0.21043>.
- Gao, Y. C., and M. F. Liu, 2013: Evaluation of high-resolution satellite precipitation products using rain gauge observations over the Tibetan Plateau. *Hydrol. Earth Syst. Sci.*, **17**, 837–849, doi:10.5194/hess-17-837-2013.
- Gleeson, T., Y. Wada, M. F. P. Bierkens, and L. P. H. van Beek, 2012: Water balance of global aquifers revealed by groundwater footprint. *Nature*, **488**, 197–200, doi:10.1038/nature11295.
- Gong, D.-Y., and C.-H. Ho, 2002: Shift in the summer rainfall over the Yangtze River valley in the late 1970s. *Geophys. Res. Lett.*, **29**, doi:10.1029/2001GL014523.
- Halley, E., 1686: An historical account of the trade winds, and monsoons, observable in the seas between and near the tropicks, with an attempt to assign the phisical cause of the said winds. *Philos. Trans. Roy. Soc. London*, **16**, 153–168, doi:10.1098/rstl.1686.0026.
- Han, W., W. T. Liu, and J. Lin, 2006: Impact of atmospheric sub-monthly oscillations on sea surface temperature of the tropical Indian Ocean. *Geophys. Res. Lett.*, **33**, L03609, doi:10.1029/2005GL025082.
- Hansen, J., and S. Lebedeff, 1987: Global trends of measured surface air temperature. *J. Geophys. Res.*, **92**, 13345–13372, doi:10.1029/JD092iD11p13345.
- Hoerling, M., A. Kumar, and M. Zhong, 1997: El Niño, La Niña, and the nonlinearity of their teleconnections. *J. Climate*, **10**, 1769–1786, doi:10.1175/1520-0442(1997)010<1769:ENOLNA>2.0.CO;2.
- Holton, J. R., 2004: *An Introduction to Dynamic Meteorology*. 4th ed. Academic Press, 535 pp.
- Hourdin, F., and Coauthors, 2006: The LMDZ4 general circulation model: Climate performance and sensitivity to parametrized physics with emphasis on tropical convection. *Climate Dyn.*, **27**, 787–813, doi:10.1007/s00382-006-0158-0.
- , and Coauthors, 2013: LMDZ5B: The atmospheric component of the IPSL climate model with revisited parameterizations for clouds and convection. *Climate Dyn.*, **40**, 2193–2222, doi:10.1007/s00382-012-1343-y.
- Hurley, J. V., and W. R. Boos, 2013: Interannual variability of monsoon precipitation and subcloud equivalent potential temperature. *J. Climate*, **26**, 9507–9527, doi:10.1175/JCLI-D-12-00229.1.
- Husak, G. J., J. Michaelsen, and C. Funk, 2007: Use of the gamma distribution to represent monthly rainfall in Africa for drought monitoring applications. *Int. J. Climatol.*, **27**, 935–944, doi:10.1002/joc.1441.
- Iguchi, T., T. Kozu, J. Kwiatkowski, R. Meneghini, J. Awaka, and K. Okamoto, 2009: Uncertainties in the rain profiling algorithm for the TRMM Precipitation Radar. *J. Meteor. Soc. Japan*, **87A**, 1–30, doi:10.2151/jmsj.87A.1.
- Ihara, C., Y. Kushnir, M. A. Cane, and V. H. de la Peña, 2007: Indian summer monsoon rainfall and its link with ENSO and Indian Ocean climate indices. *Int. J. Climatol.*, **27**, 179–187, doi:10.1002/joc.1394.
- Jhun, J.-G., and E.-J. Lee, 2004: A new East Asian winter monsoon index and associated characteristics of the winter monsoon. *J. Climate*, **17**, 711–726, doi:10.1175/1520-0442(2004)017<0711:ANEAWM>2.0.CO;2.
- Jiménez Cisneros, B. E., and Coauthors, 2014: Freshwater resources. *Climate Change 2014: Impacts, Adaptation, and Vulnerability*. C. Field et al., Eds., Cambridge University Press, 229–269.
- Kaiser, H. F., 1958: The varimax criterion for analytic rotation in factor analysis. *Psychometrika*, **23**, 187–200, doi:10.1007/BF02289233.
- Kansakar, S. R., D. M. Hannah, J. Gerrard, and G. Rees, 2004: Spatial pattern in the precipitation regime of Nepal. *Int. J. Climatol.*, **24**, 1645–1659, doi:10.1002/joc.1098.
- Kennedy, J. J., N. A. Rayner, R. O. Smith, D. E. Parker, and M. Saunby, 2011a: Reassessing biases and other uncertainties in sea surface temperature observations measured in situ since 1850: 1. Measurement and sampling. *J. Geophys. Res.*, **116**, D14103, doi:10.1029/2010JD015218.
- , —, —, —, and —, 2011b: Reassessing biases and other uncertainties in sea surface temperature observations measured in situ since 1850: 2. Biases and homogenization. *J. Geophys. Res.*, **116**, D14104, doi:10.1029/2010JD015220.
- Kosaka, Y., S.-P. Xie, and H. Nakamura, 2011: Dynamics of interannual variability in summer precipitation over East Asia. *J. Climate*, **24**, 5435–5453, doi:10.1175/2011JCLI4099.1.
- , J. S. Chowdary, S.-P. Xie, Y.-M. Min, and J.-Y. Lee, 2012: Limitations of seasonal predictability for summer climate over East Asia and the northwestern Pacific. *J. Climate*, **25**, 7574–7589, doi:10.1175/JCLI-D-12-00009.1.
- Krishnamurthy, V., and J. Shukla, 2000: Intraseasonal and interannual variability of rainfall over India. *J. Climate*, **13**, 4366–4377, doi:10.1175/1520-0442(2000)013<0001:IAIVOR>2.0.CO;2.
- , and R. S. Ajayamohan, 2010: Composite structure of monsoon low pressure systems and its relation to Indian rainfall. *J. Climate*, **23**, 4285–4305, doi:10.1175/2010JCLI2953.1.
- Krishnamurti, T. N., and P. Ardanuy, 1980: The 10 to 20-day westward propagating mode and “breaks in the monsoons.” *Tellus*, **32**, 15–26, doi:10.1111/j.2153-3490.1980.tb01717.x.
- Krishnan, R., and M. Sugi, 2001: Baiu rainfall variability and associated monsoon teleconnections. *J. Meteor. Soc. Japan*, **79**, 851–860, doi:10.2151/jmsj.79.851.
- , C. Zhang, and M. Sugi, 2000: Dynamics of breaks in the Indian summer monsoon. *J. Atmos. Sci.*, **57**, 1354–1372, doi:10.1175/1520-0469(2000)057<1354:DOBITI>2.0.CO;2.
- Kumar, K. K., B. Rajagopalan, M. Hoerling, G. Bates, and M. Cane, 2006: Unraveling the mystery of Indian monsoon failure during El Niño. *Science*, **314**, 115–119, doi:10.1126/science.1131152.

- Kumar, V., and R. Krishnan, 2005: On the association between the Indian summer monsoon and the tropical cyclone activity over northwest Pacific. *Curr. Sci.*, **88**, 602–612.
- Lau, K., K. Kim, and S. Yang, 2000: Dynamical and boundary forcing characteristics of regional components of the Asian summer monsoon. *J. Climate*, **13**, 2461–2482, doi:10.1175/1520-0442(2000)013<2461:DABFCO>2.0.CO;2.
- Lee, J.-E., C. Risi, I. Y. Fung, J. Worden, R. A. Scheepmaker, B. Lintner, and C. Frankenberg, 2012: Asian monsoon hydrometeorology from TES and SCIAMACHY water vapor isotope measurements and LMDZ simulations: Implications for speleothem climate record interpretation. *J. Geophys. Res.*, **117**, D15112, doi:10.1029/2011JD017133.
- Lei, Y., B. Hoskins, and J. Slingo, 2014: Natural variability of summer rainfall over China in HadCM3. *Climate Dyn.*, **42**, 417–432, doi:10.1007/s00382-013-1726-8.
- Li, C., and M. Yanai, 1996: The onset and interannual variability of the Asian summer monsoon in relation to land–sea thermal contrast. *J. Climate*, **9**, 358–375, doi:10.1175/1520-0442(1996)009<0358:TOAIVO>2.0.CO;2.
- Li, Z., W. Yu, T. Li, V. S. N. Murty, and F. Tangang, 2013: Bimodal character of cyclone climatology in the Bay of Bengal modulated by monsoon seasonal cycle. *J. Climate*, **26**, 1033–1046, doi:10.1175/JCLI-D-11-00627.1.
- Liu, K. S., and J. C. L. Chan, 2003: Climatological characteristics and seasonal forecasting of tropical cyclones making landfall along the South China coast. *Mon. Wea. Rev.*, **131**, 1650–1662, doi:10.1175/2554.1.
- Liu, Y., and Y. Ding, 2008: Teleconnection between the Indian summer monsoon onset and the Meiyu over the Yangtze River Valley. *Sci. China*, **51D**, 1021–1035, doi:10.1007/s11430-008-0073-9.
- Livezey, R. E., and W. Y. Chen, 1983: Statistical field significance and its determination by Monte Carlo techniques. *Mon. Wea. Rev.*, **111**, 46–59, doi:10.1175/1520-0493(1983)111<0046:SFSAD>2.0.CO;2.
- Lorenz, E. N., 1956: Empirical orthogonal functions and statistical weather prediction. Statistical Forecasting Project Scientific Rep. 1, Massachusetts Institute of Technology, 49 pp.
- Luo, Y., R. Zhang, W. Qian, Z. Luo, and X. Hu, 2011: Intercomparison of deep convection over the Tibetan Plateau–Asian monsoon region and subtropical North America in boreal summer using *CloudSat*/CALIPSO data. *J. Climate*, **24**, 2164–2177, doi:10.1175/2010JCLI4032.1.
- Mantua, N. J., and S. R. Hare, 2002: The Pacific decadal oscillation. *J. Oceanogr.*, **58**, 35–44, doi:10.1023/A:1015820616384.
- Medina, S., R. A. Houze, A. Kumar, and D. Niyogi, 2010: Summer monsoon convection in the Himalayan region: Terrain and land cover effects. *Quart. J. Roy. Meteor. Soc.*, **136**, 593–616, doi:10.1002/qj.601.
- Mishra, V., B. V. Smoliak, D. P. Lettenmaier, and J. M. Wallace, 2012: A prominent pattern of year-to-year variability in Indian summer monsoon rainfall. *Proc. Natl. Acad. Sci. USA*, **109**, 7213–7217, doi:10.1073/pnas.1119150109.
- Molnar, P., and K. A. Emanuel, 1999: Temperature profiles in radiative–convective equilibrium above surfaces at different heights. *J. Geophys. Res.*, **104**, 24 265–24 271, doi:10.1029/1999JD900485.
- , W. R. Boos, and D. S. Battisti, 2010: Orographic controls on climate and paleoclimate of Asia: Thermal and mechanical roles for the Tibetan Plateau. *Annu. Rev. Earth Planet. Sci.*, **38**, 77–102, doi:10.1146/annurev-earth-040809-152456.
- Mooley, D. A., 1973: Gamma distribution probability model for Asian summer monsoon monthly rainfall. *Mon. Wea. Rev.*, **101**, 160–176., doi:10.1175/1520-0493(1973)101<0160:GDPMFA>2.3.CO;2.
- Murakami, T., and W.-G. Huang, 1984: Orographic effects of the Tibetan Plateau on the rainfall variations over central China during the 1979 summer. *J. Meteor. Soc. Japan*, **62**, 895–909.
- Nie, J., W. R. Boos, and Z. Kuang, 2010: Observational evaluation of a convective quasi-equilibrium view of monsoons. *J. Climate*, **23**, 4416–4428, doi:10.1175/2010JCLI3505.1.
- North, G. R., T. L. Bell, R. F. Cahalan, and F. J. Moeng, 1982: Sampling errors in the estimation of empirical orthogonal functions. *Mon. Wea. Rev.*, **110**, 699–706, doi:10.1175/1520-0493(1982)110<0699:SEITEO>2.0.CO;2.
- Parthasarathy, B., A. Munot, and D. Kothawale, 1994: All-India monthly and seasonal rainfall series: 1871–1993. *Theor. Appl. Climatol.*, **49**, 217–224, doi:10.1007/BF00867461.
- Pausata, F. S. R., D. S. Battisti, K. H. Nisancioglu, and C. M. Bitz, 2011: Chinese stalagmite $\delta^{18}\text{O}$ controlled by changes in the Indian monsoon during a simulated Heinrich event. *Nat. Geosci.*, **4**, 474–480, doi:10.1038/ngeo1169.
- Peña-Arancibia, J. L., A. I. J. M. van Dijk, L. J. Renzullo, and M. Mulligan, 2013: Evaluation of precipitation estimation accuracy in reanalyses, satellite products, and an ensemble method for regions in Australia and South and East Asia. *J. Hydrometeorol.*, **14**, 1323–1333, doi:10.1175/JHM-D-12-0132.1.
- Plumb, R. A., and A. Y. Hou, 1992: Response of a zonally symmetric atmosphere to subtropical thermal forcing. *J. Atmos. Sci.*, **49**, 1790–1799, doi:10.1175/1520-0469(1992)049<1790:TROAZS>2.0.CO;2.
- Preisendorfer, R. W., F. W. Zwiers, and T. P. Barnett, 1981: *Foundations of Principal Component Selection Rules*. SIO Reference Series 81-4, Scripps Institution of Oceanography, 192 pp.
- Privé, N. C., and R. A. Plumb, 2007a: Monsoon dynamics with interactive forcing. Part I: Axisymmetric studies. *J. Atmos. Sci.*, **64**, 1417–1430, doi:10.1175/JAS3916.1.
- , and —, 2007b: Monsoon dynamics with interactive forcing. Part II: Impact of eddies and asymmetric geometries. *J. Atmos. Sci.*, **64**, 1431–1442, doi:10.1175/JAS3917.1.
- Qiu, J., 2013: Monsoon melee. *Science*, **340**, 1400–1401, doi:10.1126/science.340.6139.1400.
- Rajagopalan, B., and P. Molnar, 2013: Signatures of Tibetan Plateau heating on Indian summer monsoon rainfall variability. *J. Geophys. Res. Atmos.*, **118**, 1170–1178, doi:10.1002/jgrd.50124.
- Rajeevan, M., J. Bhate, J. D. Kale, and B. Lal, 2006: High resolution daily gridded rainfall data for the Indian region: Analysis of break and active monsoon spells. *Curr. Sci.*, **91**, 296–306.
- Risi, C., S. Bony, F. Vimeux, and J. Jouzel, 2010: Water-stable isotopes in the LMDZ4 general circulation model: Model evaluation for present-day and past climates and applications to climatic interpretations of tropical isotopic records. *J. Geophys. Res.*, **115**, D12118, doi:10.1029/2009JD013255.
- Rodwell, M. J., and B. J. Hoskins, 2001: Subtropical anticyclones and summer monsoons. *J. Climate*, **14**, 3192–3211, doi:10.1175/1520-0442(2001)014<3192:SAASM>2.0.CO;2.
- Romatschke, U., and R. A. Houze, 2011: Characteristics of precipitating convective systems in the South Asian monsoon. *J. Hydrometeorol.*, **12**, 3–26, doi:10.1175/2010JHM1289.1.
- Saha, K., F. Sanders, and J. Shukla, 1981: Westward propagating predecessors of monsoon depressions. *Mon. Wea. Rev.*, **109**, 330–343, doi:10.1175/1520-0493(1981)109<0330:WPPOMD>2.0.CO;2.
- Saji, N. H., B. N. Goswami, P. N. Vinayachandran, and T. Yamagata, 1999: A dipole mode in the tropical Indian Ocean. *Nature*, **401**, 360–363.

- Sampe, T., and S.-P. Xie, 2010: Large-scale dynamics of the meiyu-baiu rainband: Environmental forcing by the westerly jet. *J. Climate*, **23**, 113–134, doi:10.1175/2009JCLI3128.1.
- Schiemann, R., D. Lüthi, and C. Schär, 2009: Seasonality and interannual variability of the westerly jet in the Tibetan Plateau region. *J. Climate*, **22**, 2940–2957, doi:10.1175/2008JCLI2625.1.
- Schneider, T., and S. Bordoni, 2008: Eddy-mediated regime transitions in the seasonal cycle of a Hadley circulation and implications for monsoon dynamics. *J. Atmos. Sci.*, **65**, 915–934, doi:10.1175/2007JAS2415.1.
- Shen, Y., P. Zhao, Y. Pan, and J. Yu, 2014: A high spatiotemporal gauge-satellite merged precipitation analysis over China. *J. Geophys. Res. Atmos.*, **119**, 3063–3075, doi:10.1002/2013JD020686.
- Sikka, D. R., 1977: Some aspects of the life history, structure and movement of monsoon depressions. *Pure Appl. Geophys.*, **115**, 1501–1529, doi:10.1007/BF00874421.
- Singh, D., M. Tsiang, B. Rajaratnam, and N. S. Diffenbaugh, 2014: Observed changes in extreme wet and dry spells during the South Asian summer monsoon season. *Nat. Climate Change*, **4**, 456–461, doi:10.1038/nclimate2208.
- Smith, T. M., R. W. Reynolds, T. C. Peterson, and J. Lawrimore, 2008: Improvements to NOAA's historical merged land-ocean surface temperature analysis (1880–2006). *J. Climate*, **21**, 2283–2296, doi:10.1175/2007JCLI2100.1.
- Song, F., T. Zhou, and Y. Qian, 2014: Responses of East Asian summer monsoon to natural and anthropogenic forcings in the 17 latest CMIP5 models. *Geophys. Res. Lett.*, **41**, 596–603, doi:10.1002/2013GL058705.
- Tao, S.-Y., and Y.-H. Ding, 1981: Observational evidence of the influence of the Qinghai-Xizang (Tibet) Plateau on the occurrence of heavy rain and severe convective storms in China. *Bull. Amer. Meteor. Soc.*, **62**, 23–30, doi:10.1175/1520-0477(1981)062<0023:OEOTIO>2.0.CO;2.
- Tian, S.-F., and T. Yasunari, 1998: Climatological aspects and mechanism of spring persistent rains over central China. *J. Meteor. Soc. Japan*, **76**, 57–71.
- Tong, K., F. Su, D. Yang, L. Zhang, and Z. Hao, 2014: Tibetan Plateau precipitation as depicted by gauge observations, re-analyses and satellite retrievals. *Int. J. Climatol.*, **34**, 265–285, doi:10.1002/joc.3682.
- Trenberth, K. E., 1991: Climate diagnostics from global analyses: Conservation of mass in ECMWF analyses. *J. Climate*, **4**, 707–722, doi:10.1175/1520-0442(1991)004<0707:CDFGAC>2.0.CO;2.
- Vecchi, G., and D. Harrison, 2002: Monsoon breaks and subseasonal sea surface temperature variability in the Bay of Bengal. *J. Climate*, **15**, 1485–1493, doi:10.1175/1520-0442(2002)015<1485:MBASS>2.0.CO;2.
- Wang, B., and LinHo, 2002: Rainy season of the Asian–Pacific summer monsoon. *J. Climate*, **15**, 386–398, doi:10.1175/1520-0442(2002)015<0386:RSOTAP>2.0.CO;2.
- Wang, C.-C., G. T.-J. Chen, H.-L. Huang, R. E. Carbone, and S.-W. Chang, 2012: Synoptic conditions associated with propagating and nonpropagating cloud/rainfall episodes during the warm season over the East Asian continent. *Mon. Wea. Rev.*, **140**, 721–747, doi:10.1175/MWR-D-11-00067.1.
- Wang, S.-Y., and R. R. Gillies, 2013: Influence of the Pacific quasi-decadal oscillation on the monsoon precipitation in Nepal. *Climate Dyn.*, **40**, 95–107, doi:10.1007/s00382-012-1376-2.
- Wilks, D. S., 2006: *Statistical Methods in the Atmospheric Sciences*. Academic Press, 627 pp.
- Wu, G., and Coauthors, 2007: The influence of mechanical and thermal forcing by the Tibetan Plateau on Asian climate. *J. Hydrometeorol.*, **8**, 770–789, doi:10.1175/JHM609.1.
- , Y. Liu, B. He, Q. Bao, A. Duan, and F.-F. Jin, 2012: Thermal controls on the Asian summer monsoon. *Sci. Rep.*, **2**, 404, doi:10.1038/srep00404.
- Wu, H., X. Zhang, X. Li, G. Li, and Y. Huang, 2015: Seasonal variations of deuterium and oxygen-18 isotopes and their response to moisture source for precipitation events in the subtropical monsoon region. *Hydrol. Processes*, **29**, 90–102, doi:10.1002/hyp.10132.
- Xie, S.-P., H. Xu, N. H. Saji, Y. Wang, and W. T. Liu, 2006: Role of narrow mountains in large-scale organization of Asian monsoon convection. *J. Climate*, **19**, 3420–3429, doi:10.1175/JCLI3777.1.
- , K. Hu, J. Hafner, H. Tokinaga, Y. Du, G. Huang, and T. Sampe, 2009: Indian Ocean capacitor effect on Indo-western Pacific climate during the summer following El Niño. *J. Climate*, **22**, 730–747, doi:10.1175/2008JCLI2544.1.
- Xu, W., and E. J. Zipser, 2011: Diurnal variations of precipitation, deep convection, and lightning over and east of the eastern Tibetan Plateau. *J. Climate*, **24**, 448–465, doi:10.1175/2010JCLI3719.1.
- Yang, X., T. Yao, W. Yang, W. Yu, and D. Qu, 2011: Co-existence of temperature and amount effects on precipitation $\delta^{18}\text{O}$ in the Asian monsoon region. *Geophys. Res. Lett.*, **38**, L21809, doi:10.1029/2011GL049353.
- , B. Xu, W. Yang, and D. Qu, 2012: The Indian monsoonal influence on altitude effect of $\delta^{18}\text{O}$ in surface water on southeast Tibetan Plateau. *Sci. China Earth Sci.*, **55**, 438–445, doi:10.1007/s11430-011-4342-7.
- Yao, T., H. Zhou, and X. Yang, 2009: Indian monsoon influences altitude effect of $\delta^{18}\text{O}$ in precipitation/river water on the Tibetan Plateau. *Chin. Sci. Bull.*, **54**, 2724–2731, doi:10.1007/s11434-009-0497-4.
- , and Coauthors, 2013: A review of climatic controls on $\delta^{18}\text{O}$ in precipitation over the Tibetan Plateau: Observations and simulations. *Rev. Geophys.*, **51**, 525–548, doi:10.1002/rog.20023.
- Yasunari, T., and T. Miwa, 2006: Convective cloud systems over the Tibetan Plateau and their impact on meso-scale disturbances in the Meiyu/Baiu frontal zone—A case study in 1998. *J. Meteor. Soc. Japan*, **84**, 783–803, doi:10.2151/jmsj.84.783.
- Yatagai, A., K. Kamiguchi, O. Arakawa, A. Hamada, N. Yasutomi, and A. Kitoh, 2012: APHRODITE: Constructing a long-term daily gridded precipitation dataset for Asia based on a dense network of rain gauges. *Bull. Amer. Meteor. Soc.*, **93**, 1401–1415, doi:10.1175/BAMS-D-11-00122.1.
- Yeh, T.-C., S.-Y. Dao, and M.-T. Li, 1959: The abrupt change of circulation over the Northern Hemisphere during June and October. *The Atmosphere and the Sea in Motion*, B. Bolin, Ed., Rockefeller Institute Press, 249–267.
- Yoon, J.-H., and T.-C. Chen, 2005: Water vapor budget of the Indian monsoon depression. *Tellus*, **57A**, 770–782, doi:10.1111/j.1600-0870.2005.00145.x.
- Zhang, Y., D. Wang, P. Zhai, G. Gu, and J. He, 2013: Spatial distributions and seasonal variations of tropospheric water vapor content over the Tibetan Plateau. *J. Climate*, **26**, 5637–5654, doi:10.1175/JCLI-D-12-00574.1.
- Zhao, T., and A. Yatagai, 2014: Evaluation of TRMM 3B42 product using a new gauge-based analysis of daily precipitation over China. *Int. J. Climatol.*, **34**, 2749–2762, doi:10.1002/joc.3872.
- Zhou, T., R. Yu, H. Chen, A. Dai, and Y. Pan, 2008: Summer precipitation frequency, intensity, and diurnal cycle over China: A comparison of satellite data with rain gauge observations. *J. Climate*, **21**, 3997–4010, doi:10.1175/2008JCLI2028.1.